Chromatin accessibility dynamics of neurogenic niche cells reveal a reversible decline in neural stem cell migration during aging

Robin W. Yeo[1], Olivia Y. Zhou[1,2,3], Brian Zhong[4], Mahfuza Sharmin[1], Tyson J. Ruetz[1], Anshul Kundaje[1,5], Alexander R. Dunn[4], Anne Brunet[1,6,*]

Affiliations

[1] Department of Genetics, Stanford University, Stanford, CA, USA

[2] Stanford Biophysics Program, Stanford University, Stanford, CA, USA

[3] Stanford Medical Scientist Training Program, Stanford University, Stanford, CA, USA

[4] Department of Chemical Engineering, Stanford University, Stanford, CA, USA

[5] Department of Computer Science, Stanford University, Stanford, CA, USA

[6] Glenn Laboratories for the Biology of Aging, Stanford University, Stanford, CA, USA

[*]email: abrunet1@stanford.edu

Abstract

Aging is accompanied by a deterioration in the regenerative and repair potential of stem cell regions in the brain. However, the mechanisms underlying this decline are largely unknown. Here we profile the chromatin landscape of five different cell types freshly isolated from the subventricular zone neurogenic niche of young and old mice. We find that chromatin states exhibit distinct changes with aging in different cell types. Notably, the chromatin of quiescent neural stem cells (NSCs) becomes more repressed with age whereas that of proliferative, activated NSCs becomes more open. Surprisingly, these opposing age-related chromatin changes involve cell adhesion and migration pathways. We experimentally validate that quiescent and activated NSCs exhibit opposite migratory deficits during aging. Quiescent NSCs become more migratory during aging, whereas activated NSCs and progeny become less migratory and less able to mobilize out of the niche *in vivo* during aging. The cellular mechanism by which aging impairs the migration of activated NSCs and progeny involves increased occurrence of force-producing focal adhesions. Inhibiting the cytoskeletal-regulating kinase ROCK in old activated NSCs and progenitors eliminates cell adhesive forces and boosts migration speed, reverting these cells to a more youthful migratory state. Our work has important implications for restoring the migratory potential of NSCs during aging and brain injury.

47 **Main text**

48

49 The adult brain contains regenerative neural stem cell (NSC) niches, with progenitors that
50 can migrate to distal brain regions to generate new neurons and glial cells[1]. The regenerative
51 potential of stem cell regions in the brain declines with age, and this is accompanied by a
52 corresponding deterioration in aspects of sensory and cognitive function and in repair ability[2-6].
53 The subventricular zone (SVZ) neurogenic niche provides an excellent paradigm for studying
54 NSC function and migration during aging. In this niche, quiescent NSCs line the ventricular
55 wall[7-9]. Quiescent NSCs can activate and in turn generate progenitors and neuroblasts that
56 migrate towards the olfactory bulb to produce new neurons[10]. Subventricular zone NSC progeny
57 also migrate to sites of injury to mitigate damage by generating new neurons[11] and astrocytes[12].
58 Both the regenerative potential and repair abilities of the SVZ neurogenic region deteriorate with
59 age[13-16]. But the mechanisms underlying regenerative decline during aging – and how defects in
60 migratory potential might be involved – remain largely unknown.

61

62 Epigenomic changes that affect chromatin states play an important role in the regulation
63 of cell fate[17] and aging[18]. So far, however, epigenomic studies of NSCs have been limited to
64 whole tissues *in vivo*[19] or to culture systems[20-22], and age-dependent epigenomic changes in
65 different cell types of the neurogenic niche *in vivo* are unknown. While several cellular and
66 signaling defects in neurogenic niches during aging have been uncovered by transcriptomic
67 studies[23-26], changes to the chromatin landscape of NSCs could have a longer-lasting impact on
68 the progeny and reveal features of aging that were previously undetected. Identifying chromatin

changes in different cell types from the neurogenic niche during aging could help reverse age-dependent defects in regeneration and repair and counter brain aging.

The chromatin landscape of five cell types in the SVZ neurogenic region reveals opposing chromatin changes with age in quiescent and activated NSCs involving cell adhesion and migration pathways

To determine the impact of aging on the chromatin landscape of cells in the neurogenic niche *in vivo*, we generated chromatin accessibility profiles from five distinct cell types freshly isolated from the subventricular zone (SVZ) neurogenic niche of young and old mice. To this end, we aged cohorts of transgenic mice expressing green fluorescent protein driven by the promoter for glial fibrillary acidic protein (GFAP-GFP), which allows the isolation of different cell types by fluorescent activated cell sorting (FACS)[27]. The SVZ neurogenic regions of young (3-5 months old) and old (20-24 months old) GFAP-GFP mice were micro-dissected, and five cell populations from this neurogenic niche were freshly isolated by FACS[27,28] – endothelial cells, astrocytes, quiescent NSCs (qNSCs), activated NSCs (aNSCs), and neural progenitor cells (NPCs) (Fig. 1a, Extended Data Fig. 1a). To assess chromatin accessibility genome-wide on these rare cell populations (~100-1000 cells per individual), we used ATAC-seq[29-33] (Fig. 1a). We verified that ATAC-seq libraries across all conditions exhibited stereotypical 147-bp nucleosome periodicity (Extended Data Fig. 1b) and strong enrichment of accessibility around transcription start sites (TSSs) (Extended Data Fig. 1c). Principal component analysis (PCA) (Fig. 1b) and hierarchical clustering (Extended Data Fig. 2a) on accessible chromatin peaks easily separated endothelial cells from other brain cells, and quiescent cells (astrocytes and qNSCs) from activated ones (aNSCs and NPCs). The locus for *Ascl1*, a neural lineage gene

involved in NSC activation[34], shows accessible chromatin peaks in all neural cell types but not in endothelial cells, and several chromatin peaks are higher in aNSCs and NPCs than in qNSCs and astrocytes (Fig. 1c), consistent with *Ascl1* mRNA expression (Extended Data Fig. 2b). Additionally, chromatin accessibility at promoters positively correlated with mRNA expression genome-wide (Extended Data Fig. 2c). Thus, these genome-wide chromatin accessibility datasets are of high quality and represent a useful resource for studying age-related chromatin changes in 5 different cell types freshly isolated from the regenerative SVZ neurogenic niche.

Chromatin accessibility allowed separation of quiescent and activated NSCs by age (Fig. 1d for PC3, Extended Data Fig. 3a for PC2). In line with transcriptional studies[25,26,28], more chromatin peaks change with age in qNSCs (7,354) than in aNSCs (2,311) (FDR < 0.05) (Extended Data Fig. 3b, Supplementary Table 3). But interestingly, chromatin accessibility could separate young and old aNSCs whereas gene expression could not (Fig. 1d), suggesting that analyzing chromatin states may reveal new genes and pathways that had not been previously implicated in NSC aging. As expected, chromatin peaks were located either at promoters or at intronic and distal regions, which are known to contain non-coding regulatory elements such as enhancers (Fig. 1e). Performing PCA exclusively on distal and intronic chromatin peaks (putative enhancer-containing sites) was sufficient to separate NSCs based on age (Fig. 1f, Extended Data Fig. 3c,d), whereas chromatin accessibility at promoter regions alone was not (Extended Data Fig. 3e), suggesting that non-coding regulatory elements may be particularly sensitive to changes during aging.

Surprisingly, aging had opposing effects on chromatin accessibility dynamics in qNSCs and aNSCs. While most dynamic peaks in activated cells open with age, most dynamic peaks in quiescent cells closed with age (Fig. 1g). Likewise, the genome-wide chromatin landscape of old aNSCs contained more accessible chromatin peaks but less nucleosomes than that of young aNSCs while the opposite was true for qNSCs (Extended Data Fig. 3f,g). Chromatin peaks that dynamically change with age in qNSCs and aNSCs were almost entirely distal or intronic (Extended data Fig. 3h, Supplementary Table 3). Thus, the chromatin of activated NSCs becomes more permissive with age while the chromatin of their quiescent counterparts becomes more repressed, and these changes occur in putative enhancer-containing regions.

Gene Ontology (GO) biological pathway enrichment on qNSC and aNSC genes with regulatory regions that exhibited differential accessibility with age revealed cell adhesion and migration as defining hallmarks of aging in both qNSCs and aNSCs. Old qNSCs had decreased chromatin accessibility at pathways involved in promoting cell adhesion and inhibiting cell migration ("response to forskolin", "cAMP-mediated signaling", "negative regulation of cell motility", "cell-cell adhesion (plasma membrane)" (Fig. 1h, Supplementary Table 4). Conversely, old aNSCs had increased chromatin accessibility at regulatory regions of genes associated with increased cell adhesion ("cell-cell adhesion (cadherins)", "homophilic cell adhesion (plasma membrane)", "adherens junction organization") compared to young aNSCs (Fig. 1i, Supplementary Table 4). Consistently, young qNSCs and old aNSCs were grouped together based largely on cell adhesion pathways along the principal component 2 (PC2) axis (Extended data Fig. 4a, Supplementary Table 6,7). These opposing changes in qNSCs and aNSCs during aging are unlikely to be solely due to increased heterogeneity of cell populations

with age because they were also observed in scRNA-seq (Fig. 2d below) and *in vivo* brain sections (Fig. 3a-c below). Thus, aging has opposing effects on the global chromatin landscape of qNSCs and aNSCs, including changes to chromatin accessibility in regulatory regions involved in cell adhesion and migration.

The opposing chromatin changes in old quiescent and activated NSCs with aging are associated with functional defects in cell adhesion and migration

We next examined age-dependent changes in chromatin accessibility and mRNA expression of specific genes involved in cell adhesion and migration. Old qNSCs freshly isolated from the brain showed reduced chromatin accessibility at regulatory regions of cell adhesion genes, including *Cdhr3* (Cadherin Related Family Member 3) (Fig. 2a, b). In contrast, old aNSCs exhibit increased chromatin accessibility at regulatory regions of cell adhesion genes, including cadherins and *Pcdh18* (proto-cadherin 18) (Fig. 2a, b), overlapping with a number of adhesion genes enriched in young qNSCs (Extended Data Fig. 4b). Old NPCs also exhibit increased accessibility at adhesion pathways with age (Extended Data Fig. 4c, Supplementary Table 4), indicating that some of these age-related changes are preserved in downstream progeny. Motif enrichment analysis using a deep learning approach (DeepLift[35] and TF-MoDISCO[36,37], see Methods) identified the motifs for NFI transcription factors NFIB and NFIC among the most enriched within the differentially accessible chromatin regions that close with age in qNSCs and open with age in aNSCs freshly isolated from the brain (Fig. 2c). The NFI transcription factor family regulates cellular adhesion pathways in NSCs[20], and NFI isoforms affect cellular migration[38]. Hence, open chromatin dynamically changes in an opposing manner at regulatory regions of genes that contain binding sites for a key cell adhesion transcription factor.

Importantly, re-analysis of single-cell RNA-seq from the young and old neurogenic SVZ niche[25] showed that old qNSCs/astrocytes have decreased expression of genes involved in cell adhesion pathways compared to their young counterparts while old aNSCs/NPCs exhibit increased expression of cell adhesion genes compared to their young counterparts (Fig. 2d). Furthermore, changes in NSC adhesion during aging are unlikely to be explained solely by differences in cell cycle status, as cell adhesion and cell cycle signatures could be uncoupled at the single cell level (Extended Data Fig. 5). Thus, in quiescent and activated NSCs, aging leads to opposing changes in the chromatin accessibility and mRNA expression of genes involved in cell adhesion.

Our chromatin dynamics results predict that the adhesive properties of NSCs change with age. To directly test if aging functionally impacts the migratory properties of NSCs in an opposing manner, we used a culture system for quiescent NSCs and proliferative NSCs (a mix of aNSCs/NPCs)[20,28,39-41](Fig. 2e,f). We verified that the chromatin landscape of cultured NSCs was similar to that of freshly isolated NSCs (Extended Data Fig. 6a-e, Supplementary Tables 3,4,5), notably in its age-related changes to cell adhesion and migration pathways (Fig. 2g,h). To quantify NSC migration in culture, we performed continuous live-cell imaging of cultured NSCs over the course of 20 hours (Fig. 2i). Interestingly, old qNSCs were slightly more migratory (less adhesive) compared to their young counterparts (mean velocities: young (2.998 μm/hr) vs. old (3.465 μm/hr)) (Fig. 2j, Extended Data Fig 6f), whereas old aNSCs/NPCs were less migratory (more adhesive) compared to their young counterparts (mean velocities: young (13.618 μm/hr) vs. old (9.928 μm/hr)) (Fig. 2k, Extended Data Fig. 6g). Quantifying the migration of cultured aNSCs/NPCs through Matrigel, a hydrogel composed of extracellular matrix (ECM) proteins, confirmed that aNSCs/NPCs cultured from old brains exhibit impaired migration through ECM

compared to their young counterparts (Fig. 2l,m). Hence, aging has opposing effects on the adhesive and migratory properties of quiescent and activated NSCs in culture, with qNSCs becoming less adhesive and aNSCs/NPCs becoming more adhesive in old age.

Age-dependent cell adhesion and migration defects of quiescent and activated NSCs and progenitors *in vivo*

Quiescent NSCs line the ventricles and can become activated (aNSCs) to give rise to neural progenitors (NPCs) and neuroblasts that migrate along the rostral migratory stream (RMS) to the olfactory bulb (OB)[10,42,43]. While neuroblast migration has begun to be examined in older animals[44-47], the adhesive and migratory properties of quiescent and activated NSCs and their progenitors *in vivo* during aging remain largely unstudied. As adhesion to the niche plays a key role in regulating NSC stemness and function[48], we assessed quiescent and activated NSC localization *in vivo* by immunostaining of coronal brain sections from young and old individuals (Fig. 3a,b). In old brains, quiescent NSCs and niche astrocytes (GFAP+/Ki67-) were located further away from the ventricle, while activated NSCs (GFAP+/Ki67+) were located closer to the ventricle than in young brains (Fig. 3c). Together with functional data from cultured NSCs (Fig. 2), these results suggest that quiescent NSCs become less adherent to the ventricle while activated NSCs become more adherent during aging.

We next probed the migratory properties of activated NSCs and progeny during aging *in vivo*. To this end, we injected young and old mice with the thymidine analog 5-Ethynyl-2'-deoxyuridine (EdU), which incorporates into the DNA of replicating cells, to label and trace activated NSCs and their progeny. We assessed the number of EdU-positive (EdU+) cells in the

206 SVZ niche, the migration route (RMS), and destination (OB), at a short (4 hours), mid- (2 days),
207 or long (7 days) time point after EdU injection (Fig. 3d-f, Extended Data Fig. 7a). While
208 successive rounds of cell division can dilute EdU signal[49], nucleoside analogs have been used to
209 study SVZ neurogenesis in longer time frames (31 days)[16]. In young individuals, EdU+ cells
210 were numerous in the niche and along the RMS 4 hours after EdU injection (Fig. 3g,h). After 7
211 days, young animals showed a dramatic reduction of EdU+ cells in the niche and RMS, and a
212 corresponding increase in EdU+ cells in the OB, consistent with mobilization out of the niche
213 and clearance from the RMS towards the OB (Fig. 3g-i). In old individuals, EdU+ cells were less
214 numerous, as expected[15,16,50,51] (Fig. 3f, Extended Data Fig. 7b), but they neither significantly
215 decreased in the SVZ niche after 7 days (Fig. 3j) nor increased in the OB after 7 days (Fig. 3l). In
216 the aged neurogenic niche, old EdU+ aNSCs/NPCs and neuroblasts (Extended Data Fig. 7c)
217 were located closer to the ventricle, after a 4 hour EdU pulse, than their young counterparts (Fig.
218 3m-o). These observations are consistent with an inability of old aNSCs and progeny to mobilize
219 out of the old neurogenic niche. We did observe some clearance of EdU+ cells through the old
220 RMS after 7 days (Fig. 3k), suggesting that old neuroblasts retain some motility in the RMS[44],
221 but migrate more slowly than young neuroblasts. Thus, aging impairs the tight localization of
222 quiescent NSCs to the ventricles and decreases the migratory ability of old aNSCs and
223 downstream progeny (NPCs and neuroblasts) to their distal destination *in vivo*.
224
225 **Aging increases the occurrence of force-producing focal adhesions in aNSCs/NPCs**
226 We assessed the cellular mechanisms underlying the decrease in migratory properties of
227 aNSCs and progenitors, and their increased cell adhesion, during aging. Adhesion of cells to the
228 extracellular matrix (ECM) primarily involves integrin-mediated linkage between ECM and actin

cytoskeleton (Fig. 4a). We first used immunofluorescence staining to visualize the F-actin cytoskeleton and quantify bundled actin, which contributes to cellular adhesion through the formation of stress fibers, lamellipodia, and filopodia[52,53]. Activated NSCs/NPCs cultured from old brains exhibited increased staining for bundled actin compared to young counterparts (Fig. 4b,c). Thus, the age-related migratory deficit of old cultured aNSCs/NPCs is accompanied by increased cytoskeletal assembly, which is necessary for integrin-based adhesion to the ECM.

To directly visualize the mechanical forces imparted by aNSCs/NPCs interacting with their substrate, we next leveraged Förster resonance energy transfer (FRET)-based molecular tension sensors (Fig. 4a)[54,55]. Molecular tension sensors reveal forces exerted by aNSCs/NPCs on surfaces coated with synthetic arginine-glycine-aspartate (RGD) peptides known to bind integrins and mediate adhesion[55], with higher forces corresponding to a reduction in FRET (Fig. 4a). FRET measurements revealed that aNSCs/NPCs primarily exert force though distinct focal adhesion complexes at their periphery (Fig. 4d). Consistently, bundled actin also aggregated peripherally in aNSCs/NPCs (Extended Data Fig. 8a). We quantified the adhesive force patterns for young and old cultured aNSCs/NPCs and found that their focal adhesion profiles were bimodal, with a population of cells exhibiting force-producing focal adhesions and a population with no force-producing focal adhesions (Fig. 4e,f). While aging does not significantly affect individual focal adhesion strength or area (Fig. 4e, Extended Data Fig. 8b), old aNSCs/NPCs were more likely to exhibit force-producing adhesions than young aNSCs/NPCs (Fig. 4f, Extended Data Fig. 8c-e) (P=0.0327, combined Fisher's exact test). Specifically, old aNSCs/NPCs were much more likely than young aNSCs/NPCs to exhibit force-producing adhesions when in contact with other cells (Extended Data Fig. 8f,g). Thus, a higher prevalence

of force-producing adhesions in old aNSCs/NPCs likely contributes to the functional deterioration in the migration of activated NSCs and their progeny in the aged brain.

Inhibition of ROCK boosts migration speed and eliminates focal adhesions in aNSCs/NPCs from aged brains

To identify a molecular target to modulate and potentially reverse the age-related migratory deficit of old activated NSCs and progenitors, we used Ingenuity Pathway Analysis (IPA) to enrich for signaling pathways associated with the chromatin accessibility changes seen in old aNSCs/NPCs. Pathway enrichment by IPA revealed a number of signaling pathways including some involved in cell adhesion (Fig. 5a, Supplementary Table 8), consistent with our GO analysis (see Fig. 1i). The most enriched pathway in this cluster was Gα 12/13 signaling (Fig. 5a), which regulates cell adhesion in part via Rho and Rho-associated protein kinase (ROCK)[56,57] (Fig. 5b). ROCK plays a major role in regulating the actin cytoskeleton and cell adhesion (among other phenotypes)[58], and it could serve as a molecular target to reverse the age-dependent decline in aNSC/NPC migration.

To determine if the migratory properties of old aNSCs and their progenitors could be ameliorated via modulation of the ROCK pathway, we targeted ROCK with the small molecule inhibitor Y-27632[59-66] in cultured aNSCs/NPCs. Quantification of force patterns on RGD molecular tension sensors (Fig. 5c) revealed that treating old aNSCs/NPCs with the ROCK inhibitor Y-27632 eliminated force-producing focal adhesions (Fig. 5d,e). Consistently, inhibiting ROCK in old aNSCs/NPCs also resulted in decreased staining for bundled actin (Fig. 5f,g). ROCK inhibition resulted in improved migration speed in both young and old

aNSCs/NPCs (mean velocities: young (13.618 μm/hr) vs. young + Y-27632 (20.201 μm/hr); old (9.928 μm/hr) vs. old + Y-27632 (21.691 μm/hr)) (Fig. 5h,i, Extended Data Fig. 8h, Supplementary Videos 1,2). Furthermore, inhibiting ROCK rescued the age-related decline in old aNSC/NPC migration through ECM (Fig. 5j). Together, these data indicate that inhibition of the ROCK pathway could ameliorate the age-related migratory deficit of old aNSCs and progenitors for neurogenesis and repair targets.

Discussion

Our study is the first to identify age-related genome-wide changes to the global chromatin landscape of quiescent and activated NSCs freshly isolated from the adult SVZ neurogenic niche. This analysis reveals that aging has opposing effects on the opening and closing of dynamic chromatin regions in quiescent and activated NSCs, with many of these changes affecting adhesion and migration pathways. Our study also shows for the first time that old activated NSCs and progenitors exhibit impaired migration, and that ROCK inhibition boosts the migratory ability of these cells in culture partly by decreasing the formation of force-producing adhesions. This work could uncover new strategies to restore age-dependent defects in regeneration and repair by targeting adhesive and migratory changes with age.

The chromatin landscape of quiescent NSCs becomes less open with age whereas that of activated NSCs becomes more open with age. The closing of chromatin regions with age in quiescent NSCs is consistent with findings of increased age-related repressive chromatin marks such as H3K27me3 in other quiescent stem cells[67], including quiescent muscle satellite cells[68,69] and hematopoietic stem cells[70]. The chromatin landscape of activated NSCs generally becomes

298 more permissive with age, consistent with the observation that reducing the repressive 5-
299 hydroxymethylcytosine (5hmC) mark in hippocampal NPCs mimics age-dependent defects[19].
300 Moreover, it is interesting to note that age-related chromatin changes are readily detectable in
301 activated NSCs, yet transcriptomic changes are very limited in these cells[25,26,28] and other cellular
302 systems[70-72]. Because the majority of dynamic chromatin changes that occur with age in NSCs
303 impact distal and intronic regulatory sites, which likely contain non-coding regulatory elements
304 such as enhancers, age-related chromatin changes in aNSCs may underlie longer-lasting changes
305 and manifest themselves transcriptionally more in downstream progenitors.
306
307 Cell adhesion emerged as a hallmark of NSC aging in our study. The migratory
308 properties of neuroblasts has started to be examined with age[44-47] and in the context of
309 innervating distal tumors[73]. But the changes in migration and adhesion in quiescent and activated
310 NSCs, the upstream NSC populations that give rise to migratory neuroblasts, remain largely
311 unknown. Our study reveals a dichotomy between changes to the adhesive/migratory properties
312 of quiescent and activated NSCs with age. As mechanical cell deformations affect the nucleus
313 and chromatin itself[74,75], epigenomic profiling might be especially sensitive to identifying
314 changes in the regulation of adhesion and migration in stem cells and their progeny.
315
316 A key question is the role of intrinsic factors vs. extrinsic factors in cell migration with
317 age. Age-related changes to the biomechanical properties of regenerative niches, such as
318 stiffness, have been shown to extrinsically induce age-related phenotypes[76]. Our findings in
319 cultured aNSCs/NPCs highlight the importance of intrinsic changes to cellular adhesion
320 pathways that change with age. Notably, aNSCs/NPCs isolated from an old brain retain

321 migratory impairment and increased occurence of force-producing adhesions even when
322 removed from the extrinsic effects of the niche. Understanding the contribution of intrinsic and
323 extrinsic responses, and how they influence each other during aging, will be critical to identify
324 strategies to boost regeneration and repair during aging.
325
326 Inhibiting Rho-associated kinase (ROCK), a regulator of cytoskeletal dynamics[57], with
327 the small molecule Y-27632 improves motility in aged activated NSCs and downstream
328 progenitors. Inhibition of ROCK has a profound impact on migration in a variety of cells,
329 including myoblasts, glioma cells, and microglia with different effects[77-84]. However, ROCK
330 inhibition has previously not been tested in aNSCs/NPCs during aging, and its effects on young
331 aNSCs/NPCs remain unclear: one study of human embryonic stem cell (ESC)-derived NSCs
332 showed decreased migration speed upon ROCK inhibition[85], while another study of NSCs
333 derived from postnatal and young adult mice showing increased migration speed upon ROCK
334 inhibition[64]. Here we show that ROCK inhibition eliminates focal adhesions and increases
335 migration in old aNSCs/NPCs. While ROCK has pleiotropic roles in aspects other than migration
336 (e.g. autophagy, apoptosis, vesicle dynamics, etc.), this protein kinase is a promising potential
337 target in the aging brain to restore aspects of migration notably in cases of injury and
338 neurodegenerative disease[86]. ROCK inhibitors are well tolerated in humans and have begun to be
339 studied in the context neurodegenerative disease[86] and could potentially be used to ameliorate
340 other age-dependent defects. Our study could help identify ways to restore proper migration of
341 NSCs and progenitors in the aging brain and in the context of brain injury.
342
343

Acknowledgements

We thank D. Wagh from the Stanford Functional Genomics Facility for Illumina NextSeq sequencing; the Stanford Shared FACS Facility for FACS use and support; K. Tsui and M. Bassik for assistance and use of the Incucyte Live Cell Imaging system; M. Buckley, G. A. Reeves, X. Zhao, P. P. Singh, and C.-K. Hu for their feedback and reading of the manuscript; M. Buckley, G. A. Reeves, P. P. Singh, and A. McKay for independently checking scripts used in this study; J. Butterfield for help with mouse husbandry and genotyping; and M. Bassik, J. Sage, and T. Wyss-Coray for guidance. This work was supported by P01AG036695 (A.B.), the Stanford Genome Training Program (R.W.Y.), a Stanford Graduate Fellowship (R.W.Y.), and a Genentech Foundation Pre-doctoral Fellowship (R.W.Y.).

Authors contributions

R.W.Y. and A.B. planned the study. R.W.Y. performed and analyzed all experiments, except for those indicated below. O.Y.Z. generated sections, performed immunostaining, and quantification for all *in vivo* experiments and participated in the planning of the study. B.Z. performed the RGD tension sensor experiments and analyzed the FRET data supervised by A.D.. M.S. generated the NSC deep learning model and performed motif enrichment supervised by A.K.. T.R. assisted in the *in vivo* NSC migration study. A.K. and A.D. also provided intellectual contribution. R.W.Y. and A.B. wrote the manuscript, with help from O.Y.Z., and all authors provided comments.

Competing Interests

The authors declare no competing interests.

Data availability

All raw sequencing reads and processed bam files for ATAC-seq libraries can be found under BioProject PRJNA715736.

Code availability

The code used to analyze genomic data in the current study are available in the Github repository for this paper (https://github.com/brunetlab/Yeo_RW_NSC_ATACseq).

Methods

Laboratory animals

For *in vivo* ATAC-seq libraries and immunofluorescence experiments with coronal sections, an equal number of male and female GFAP-GFP (FVB/N background) mice[87] were pooled and used. For ATAC-seq libraries generated from cultured NSCs, the SVZs from one male and one female C57BL/6 mouse obtained from the NIA Aged Rodent colony were pooled and used. For all other experiments, male C57BL/6 mice obtained from the NIA Aged Rodent colony were used. In all cases, mice were habituated for more than one week at Stanford before use. At Stanford, all mice were housed in either the Comparative Medicine Pavilion or the Neuro Vivarium, and their care was monitored by the Veterinary Service Center at Stanford University under IACUC protocols 8661.

ATAC-seq library generation from freshly isolated cells

We used fluorescence-activated cell sorting (FACS) to freshly isolate populations of endothelial cells, astrocytes, quiescent NSCs (qNSCs), activated NSCs (aNSCs), and neural progenitor cells (NPCs) from GFAP-GFP (FVB/N background) animals[87], as previously described[28]. Briefly, we micro-dissected and processed the subventricular zones from young (3-5 months old) and old (20-24 months old) GFAP-GFP mice following the previously described protocol[27] with the addition of negative gating for CD45 (hematopoietic lineage) and sorting of endothelial cells (CD31+) as previously described[28] (see Extended Data Fig. 1a). All FACS sorting was performed at the Stanford FACS facility on a BD Aria II sorter, using a 100-μm nozzle at 13.1 pounds/square inch (psi), and Flowjo (v8) software was used for data analysis. Due to the rarity

of NSC lineage cells, we pooled sorted cells from 2 young male and 2 young female GFAP-GFP mice for the young conditions (3-5 months old), and from 3 old male and 3 old female GFAP-GFP mice for the old conditions (20-24 months old). For each respective library, we sorted either 2000 astrocytes, 2000 qNSCs (with the exception of a single library which only had 1670 cells), 800-1000 aNSCs, 2000 NPCs, or 2000 endothelial cells from GFAP-GFP animals for ATAC-seq (see Supplementary Table 2). Young and old cells of the five cell types were sorted into 150 µL of NeuroBasal-A medium (Gibco, 10888-022) with penicillin-streptomycin-glutamine (Gibco, 10378-016) and 2% B27 minus vitamin A (Gibco, 12587-010) in a 96-well V-bottomed plate (Costar, 3894) and spun down at 300g for 5 min at 4°C. Sorted cells were washed with 100 µL ice-cold 1x PBS (Corning, 21-040-CV), male and female cells were pooled by age and cell type, and then spun down at 300g for 5 min at 4°C. Next, 50 µL of lysis buffer (10 mM Tris HCl pH 7.4 (Sigma, T2194), 10 mM NaCl, 3 mM $MgCl_2$ (Ambion, AM9530G), 0.10% NP-40 (Thermo, 85124)) was added to each well (alternating between young and old wells) and was immediately spun down at 500g for 10 min at 4°C. Lysis buffer was carefully aspirated and 5 µL of transposition mix (2.5 µL 2x Tagment DNA (TD) buffer, 2.25 µL nuclease-free H_2O, 0.25 µL Tn5 transposase (Illumina, FC-121-1030)) was added to each well and pipetted 6x to resuspend nuclei. Cells were incubated for 30 min at 37°C in a sealed 96-well plate and then briefly spun down at 500g for 1 min to account for evaporation. Transposed DNA was then purified using the Zymo DNA Clean & Concentrator kit (Zymo, D4014) and eluted in 20 µL of nuclease-free H_2O. PCR amplification and subsequent qPCR monitoring was performed as previously described in the original ATAC-seq protocol[29]. ATAC-seq libraries from young and old cells were amplified with 11-14 PCR cycles and then purified using the Zymo DNA Clean & Concentrator kit (Zymo, D4014) and eluted in 15 µL of nuclease-free H_2O. See below "*Library sequencing and ATAC-*

436 *seq quality control of in vivo and cultured NSCs*" for details on sequencing of ATAC-seq
437 libraries.
438
439 **Primary NSC cell culture**
440 To obtain primary cultures of adult NSCs for ATAC-seq, we micro-dissected and pooled SVZs
441 from pairs of male and female C57BL/6 mouse at a young age (3 months old) or an old age (23
442 months old) obtained from the NIA. To obtain primary cultures of adult NSCs for
443 immunofluorescence staining, migration assays, and force sensor assays, we micro-dissected the
444 SVZs from a single young C57BL/6 male (3-5 months old) or a single old C57BL/6 male (20-24
445 months old) obtained from the NIA (see Supplementary Table 1). In both cases, micro-dissected
446 SVZs were finely minced, suspended in 5 mL of PBS +0.1% Gentamicin (Thermo Fisher,
447 15710064) and spun down at 300g for 5 min at room temperature. We then dissociated SVZs by
448 enzymatic digestion using 5 mL of HBSS (Corning, 21-021-CVR) with 1% penicillin-
449 streptomycin-glutamine (Gibco, 10378-016), 1 U/mL Dispase II (STEMCELL Technologies,
450 07913), 2.5 U/mL Papain (Worthington Biochemical, LS003126), and 250 U/mL DNAse I
451 (D4527, Sigma-Aldrich), vortexed briefly, and left at 37°C for 40 min on a rotator. Following
452 digestion, the samples were spun down at 300g for 5 min at room temperature and resuspended
453 in 5 mL of NeuroBasal-A medium (Gibco, 10888-022) with 1% penicillin-streptomycin-
454 glutamine (Gibco, 10378-016) and 2% B27 minus vitamin A (Gibco, 12587-010) and triturated
455 repeatedly (20x) with 2-3 washes. Single-cell suspensions were then resuspended in "complete
456 activated media": Neurobasal-A (Gibco, 10888-022) supplemented with 2% B27 minus vitamin
457 A (Gibco, 12587-010), 1% penicillin–streptomycin–glutamine (Gibco, 10378-016), 20 ng/mL of
458 EGF (Peprotech, AF-100-15), and 20 ng/mL of bFGF (Peprotech, 100-18B). For passaging, cells

were dissociated with 1 mL Accutase (STEMCELL Technologies, 07920) for 5 min at 37°C, washed once with 5 mL 1x PBS, and resuspended in "complete activated media" for expansion. For quiescent conditions, quiescence was induced over 5-10 days by replacing "complete activated media" with "complete quiescent media": Neurobasal-A (Gibco, 10888-022) supplemented with 2% B27 minus vitamin A (Gibco, 12587-010), 1% penicillin–streptomycin–glutamine (Gibco, 10378-016), 50 ng/mL of BMP4 (Biolegend 94073), and 20 ng/mL of bFGF (Peprotech, 100-18B). For adherent cultures, we coated plates with PBS+Poly-D-Lysine (Sigma-Aldrich, P6407, 1:20) for 30-120 min at 37°C, and washed plates 4x with 1x PBS prior to seeding cells. All cell counting was performed using the Countess II FL Automated Cell Counter (Life Technologies, AMQAF1000).

ATAC-seq library generation from cultured NSCs

To establish individual primary NSC cultures for ATAC-seq, we dissected and pooled the SVZs from one male and one female C57BL/6 NIA mouse from either a young cohort (3 months old) or an old cohort (23 months old). We dissociated and cultured NSCs as described above (in the section "*Primary NSC cell culture*") to generate 4 young and 4 old biological replicates. At passage 5, NSCs were plated at a density of 1.2 million cells per 6cm PDL-coated plate in complete quiescent media for 8 days prior to sorting. At passage 7, NSCs from the same culture were plated at a density of 1.5 million cells per 6cm plate onto PDL-coated plates in complete activation media for 24 hours prior to sorting to synchronize quiescent and activated sorting experiments. Plates were washed 3x with 1x PBS. Adherent qNSCs were lifted from the plate using 1 mL of Accutase (STEMCELL Technologies, 07920) for 15 min at 37°C and adherent aNSCs/NPCs were lifted from the plate using 1 mL of Accutase (STEMCELL Technologies,

07920) for 5 min at 37°C. The Accutase (STEMCELL Technologies, 07920) cell suspension was diluted with 10 mL of 1x PBS, cells were spun down at 300g for 5 min, then resuspended in 200 µL of Neurobasal-A (Gibco, 10888-022) supplemented with 2% B27 minus vitamin A (Gibco, 12587-010), 1% penicillin–streptomycin–glutamine (Gibco, 10378-016) with propidium iodide (BioLegend, 421301, 1:5000) for live/dead staining. Cells were kept on ice during all subsequent steps.

Due to concern about differing levels of dead cells in the young vs. old cultures as well as the contaminating influence of dead cells on ATAC-seq libraries, all samples were sorted using fluorescence-activated cell sorting (FACS) based on the live gate (propidium iodide). Specifically, 10,000-15,000 live cultured qNSCs and aNSCs/NPCs (see Supplementary Table 2) were respectively sorted into 100 µL of NeuroBasal-A medium (Gibco, 10888-022) with penicillin-streptomycin-glutamine (Gibco, 10378-016) and 2% B27 minus vitamin A (Gibco, 12587-010) in a 96-well V-bottomed plate (Costar, 3894) and spun down at 300g for 5 min at 4°C. Sorted cells were washed with 100 µL ice-cold 1x PBS (Corning, 21-040-CV), and spun down at 300g for 5 min at 4°C. 50 µL of lysis buffer (10mM Tris HCl pH 7.4 (Sigma, T2194), 10mM NaCl, 3mM $MgCl_2$ (Ambion, AM9530G), 0.10% NP-40 (Thermo, 85124)) was added to each well (alternating between young and old wells) which were immediately spun down at 500g for 10 min at 4°C. Lysis buffer was carefully aspirated and 50 µL of transposition mix (12.5 µL 4x Tagment DNA (TD) buffer (gift from the Chang Lab), 35 µL nuclease-free H_2O, 2.5 µL Tn5 (gift from the Chang Lab)) was added to each well and pipetted 6x to resuspend nuclei. Cells were incubated for 30 min at 37°C in a sealed 96-well plate and then briefly spun down at 500g for 1 min to account for evaporation. Transposed DNA was then purified using the Zymo DNA Clean & Concentrator kit (Zymo, D4014) and eluted in 20 µL of nuclease-free H_2O. PCR

amplification and subsequent qPCR monitoring was performed as previously described in the original ATAC-seq protocol[29]. All libraries were amplified for 5 PCR cycles, and then an additional 4 PCR cycles (based off of qPCR amplification curves), and then purified using the Zymo DNA Clean & Concentrator kit (Zymo, D4014) and eluted in 15 μL of nuclease-free H_2O.

Library sequencing and ATAC-seq quality control of *in vivo* and cultured NSCs

We quantified individual library concentrations using a Bioanalyzer (High Sensitivity) and pooled at a concentration of 5 nM for sequencing. Multiplexed libraries were sequenced using NextSeq (400M) by the Stanford Functional Genomics Facility. To assess individual library quality, individual library paired-end FASTQ files were processed using the Kundaje Lab's ATAC-seq Pipeline (https://github.com/kundajelab/atac_dnase_pipelines) with default parameters (using "-species mm10" and including "-auto_detect_adapter").

For *in vivo* ATAC-seq libraries generated from freshly isolated SVZ cells, libraries were excluded based on insufficient read coverage (<10 million unique reads) or low peak calling (<=20,000 peaks). In general, endothelial cell libraries were of worse quality than the other four sorted cell types and we additionally censored one endothelial library with low bowtie alignment (~92%) since all other libraries had a bowtie alignment of >= 95%.The high-quality libraries were sequenced to a mean read depth of 29,187,427 unique reads (ranging from ~10-69 million reads per library) (see Supplementary Table 2).

In general, ATAC-seq library quality was much better for cultured NSCs than freshly isolated NSCs so we used a different set of metrics for quality control. For cultured NSCs, 1 library (out of 4) from each condition was excluded to due to poor quality, defined as the library with the lowest transcription start site (TSS) enrichment (<20 in all cases). Additionally, both young and

old quiescent cultures had one library that appeared highly anomalous (~2-fold greater fraction of reads in peaks (FRiP) and TSS enrichment compared to every other library) so they were additionally excluded to not confound results. The remaining 2-3 high-quality libraries per condition were sequenced to a mean read depth of 26,271,688 unique reads (ranging from ~18-42 million reads per library) (see Supplementary Table 2).

ATAC-seq pipeline and processing

Libraries that passed quality control were re-processed using the Kundaje Lab's ATAC-seq Pipeline starting from de-duplicated BAM files to call peaks per multi-replicate condition. De-duplicated, Tn5-shifted tagAlign files for each replicate were converted to BAM files (using bedToBam (v2.29.2)) and sorted (using samtools sort (v1.10)) for downstream analysis. Peaks per multi-replicate condition were selected using "overlap > optimal set" resulting in approximately 20,000-90,000 peaks per *in vivo* condition (with a mean peakset size of 65,243 peaks) and approximately 90,000-150,000 peaks per cultured NSC condition (with a mean peakset size of 118,987 peaks). To generate pooled read libraries, the 2-3 high-quality filtered, de-duplicated BAM files for each condition were merged (using samtools merge (v1.10)), sorted (using samtools sort (v1.10)), tn5-shifted (using deepTools alignmentSieve (v3.4.3)), and indexed (using samtools index (v1.10)). All analysis was performed using the *mm10* mouse genome ("TxDb.Mmusculus.UCSC.mm10.knownGene").

Transcription start site (TSS) enrichment

Transcription start site (TSS) enrichment heatmaps were generated with ngsplot.R (version 2.6.1)[88] using pooled, Tn5-shifted, sorted BAM files as inputs for each of the 10 conditions. All

551 analysis was performed using the *mm10* mouse genome
552 ("TxDb.Mmusculus.UCSC.mm10.knownGene").
553
554 **Generating consensus peaksets and count matrices**
555 To generate consensus peaksets for downstream analysis, BAM files and multi-replicate peak
556 files were loaded into a Large DBA object using Diffbind (v2.10.0)[89,90] "dba.count" with
557 parameters "minOverlap=0" and "score=DBA_SCORE_READS". We annotated peaks in the
558 consensus count matrices using the "annotatePeak" function of the package ChIPSeeker
559 (v1.18.0)[91] with parameters "tssREgion=c(-3000,3000)".
560
561 **Functional enrichment of genetic elements within global peaksets**
562 The "annotatePeak" function of ChIPSeeker (v1.18.0)[91] was used to identify the genetic element
563 identity of each chromatin peak within the multi-replicate peakset for each condition with
564 parameters (tssRegion=c(-3000, 3000), annoDb="org.Mm.eg.db"), and the annotation statistics
565 were extracted using "@annoStat". The different promoter terms "Promoter (<=1kb)",
566 "Promoter (1-2kb)", and "Promoter (2-3kb)" were manually grouped together under "Promoter",
567 and the two intron terms were manually grouped under "Intron".
568
569 **Principal Component Analysis (PCA)**
570 DESeq2 (v1.22.2)[92] was used to calculate dispersion estimates from raw consensus count
571 matrices and then variance stabilizing transformations were applied prior to visualization by
572 principal component analysis.

For *in vivo* ATAC-seq libraries generated from freshly isolated SVZ cells, PCA on all chromatin peaks was generated using the global consensus peakset of 141,970 peaks. PCA consisting of all young and old qNSC and aNSC libraries was generated using the count matrix consisting of these 87,796 peaks. Based on peak annotations, the NSC consensus peakset was sub-divided into a distal peakset (31,660 peaks), an intronic peakset (28,571 peaks), a promoter peakset (20,633), and a putative enhancer (distal+intronic) peakset (60,231 peaks). For ATAC-seq libraries generated from cultured NSCs, PCA was generated from the consensus peakset with 121,497 peaks. To compare how cultured NSCs compared to NSCs freshly isolated from the SVZ, we performed PCA on the count matrix consisting of the 11 freshly isolated NSC libraries and the 10 cultured NSC libraries (156,963 peaks).

Clustering freshly isolated ATAC-seq libraries for heatmap visualization

To cluster and visualize all ATAC-seq libraries from freshly isolated SVZ cell populations together, we generated a heatmap from the global consensus peakset (141,970 peaks) with "cor()" using the default Pearson's correlation with the R library "pheatmap" (v1.0.12).

Correlating ATAC-seq promoter accessibility and RNA-seq expression

For young and old qNSCs and aNSCs freshly isolated from the SVZ, the average (VST-normalized) chromatin accessibility value of each gene's promoter was associated with the average (VST-normalized) RNA-seq[28] expression value for that gene. Promoters were binned in deciles based on promoter accessibility and the association between promoter chromatin accessibility and associated genic mRNA expression was plotted as deciled boxplots using R (v3.5.2).

596

597 **Chromatin signal track visualization for freshly isolated NSCs**

598 Alignment tracks were visualized using IGV (v2.4.19). For each condition, the BAM file for a
599 single representative library (see Supplementary Table 2) was normalized by Reads per Kilobase
600 per Million mapped reads (RPKM-normalization) and converted to a bigwig file using deepTools
601 (v3.4.3) with the following parameters: "--extendReads 100 --normalizeUsing RPKM --binSize
602 10".

603

604 **Differential peak calling**

605 To identify differentially accessible peaks that change with age for each cell type, count matrices
606 consisting of young and old replicates within a single cell type were generated using Diffbind
607 (v2.10.0)[89,90] as described above (see *Generating consensus peaksets and count matrices*).
608 Differential peak calling was accomplished using EdgeR (v3.24.3)[93,94] with the following
609 parameters for "dba.analyze": bCorPlot=FALSE, bParallel=TRUE, bTagwise=FALSE,
610 bFullLibrarySize=TRUE, bReduceObjects=FALSE,method=DBA_EDGER". For all
611 comparisons, differential peaks were obtained using a false discovery rate (FDR) threshold of
612 0.05 (see Supplementary Table 3). Differential peaks were annotated and associated with their
613 closest gene using the "annotatePeak" function of the package ChIPSeeker (v1.18.0)[91] with
614 parameters "tssREgion=c(-3000,3000)". For the differential peaks that change with age in the
615 freshly isolated qNSC and aNSC libraries respectively, differential peaks were aligned to the
616 *mm10* chromosomes using the "covplot()" function in ChIPSeeker (v1.18.0)[91] for ease of
617 visualization. It should be noted that the opposing directionality of dynamic peak changes with

618 age was only observed in freshly isolated qNSCs and aNSCs (whereas cultured qNSCs and
619 aNSCs/NPCs both generally show an opening of chromatin peaks with age).
620
621 **Functional enrichment of genetic elements within differential NSC peaksets**
622 The differentially accessible peaks that change with age in the freshly isolated qNSC and aNSC
623 conditions respectively were separated into sets that close with age or open with age and were
624 annotated with the "annotatePeak" function of ChIPSeeker (v1.18.0)[91] with parameters
625 (tssRegion=c(-3000, 3000), annoDb="org.Mm.eg.db"). The annotation statistics from
626 "@annoStat" were manually grouped into 4 categories: "Distal Intergenic", "Intron",
627 "Promoter", and "Other".
628
629 **Nucleosome peak calling**
630 To identify whether the chromatin landscapes of young and old freshly isolated qNSCs and
631 aNSCs had different levels of heterochromatin-associated nucleosomes, we used the package
632 NucleoATAC (v0.2.1)[95]. We called nucleosome peaks from our ATAC-seq data using
633 "nucleoatac run" with parameters: "--bed" the multi-replicate peak files for each condition, "--
634 bam" pooled, down-sampled (to 30 million unique reads), Tn5-shifted BAM files, and "--fasta"
635 the mm10 Mus musculus UCSC genome. The number of nucleosome peaks for each condition
636 were taken from the "*.nucmap_combined.bed" files and plotted with R (v3.5.2).
637
638 **Gene Ontology (GO) Biological Pathway Enrichment of differentially accessible chromatin**
639 **peaks**

Differentially accessible peaks were associated with nearby genes using the ChIPSeeker (v1.18.0)[91] function "annotatePeak". Gene lists were uploaded to the online tool EnrichR[96,97] and top ranked GO terms from "GO Biological Process 2018" were extracted for pathways that change with age (see Supplementary Table 4). Selected GO terms were ranked by *P*-value and plotted for visualization in R (v3.5.2).

Gene Ontology (GO) Biological Pathway Enrichment of genes driving PC axes

In order to identify what biological processes were associated with peaks driving the principal components (PCs) in the PCA of young and old freshly isolated qNSCs and aNSCs, the top 1000 peaks driving the principal components (either negatively or positively) were extracted and associated with genes (see Supplementary Table 6). The genes (under header "Symbol") associated with these peaks were uploaded to EnrichR to identify top ranked GO terms from "GO Biological Process 2018" (see Supplementary Table 7). The top 6 GO terms for PC2 negative peaks (grouping old qNSCs and young aNSCs) and PC2 positive peaks (grouping young qNSCs and old aNSCs) were ranked by *P*-value and plotted in R (v3.5.2) for visualization.

Chromatin peak heatmaps within cell adhesion pathways

To visualize how aging affects chromatin peak accessibility associated with cell adhesion, genes associated with differential peaks that change with age in either freshly isolated qNSCs or aNSCs respectively were intersected with the "Cell Adhesion" GO gene list (GO:0007155) (http://www.informatics.jax.org). Differential peak accessibility levels were plotted as heatmaps using "pheatmap" (v1.0.12) in R (v3.5.2) (TMM-normalized read counts, scaled row-wise).

663

664 **Homer Motifs**

665 To identify transcription factors that could be involved in aging, motif enrichment was
666 performed using the Homer tool "findMotifsGenome.pl" (v4.11.1)[98] with parameters "-size
667 given -mask" on differential peak lists (only Known Motifs are reported here) (see
668 Supplementary Tables 5). Since many enriched motifs were highly redundant, selected motifs
669 were grouped by identity and plotted for visualization (ranked by p-value) in R (v3.5.2).

670

671 ***De novo*** **transcription factor binding patterns using a deep learning model and TF-**
672 **MoDISco**

673 Binary open/closed chromatin was learned using a deep learning model (Basset architecture, i.e.
674 3 convolution layers, 2 fully connected layers followed by logit)[99] for each of the young and old
675 freshly isolated cell types (except for endothelial cells which were omitted due to inferior library
676 quality). For model training, naïve overlap peaks were used as positive examples (i.e. open
677 chromatin) and sequences from the rest of the genome were used as negative examples (i.e.
678 closed chromatin). The size of each example is a 1kb sequence, each taken with 50bp strides of
679 size 200 initially and expanded to 1kb later on. Sequences with at least 50% overlap with the
680 naïve peaks are positive examples and the rest are the negative examples. Each model was tested
681 on chromosome 1 and trained on rest of the chromosomes. Their genome-wide performance
682 ranged from 0.22 to 0.5 auPRC (Area Under precision recall curve) depending on the imbalance
683 ratio of positive and negative examples for the sequence. Notably, amongst all of the different
684 conditions, model performance for young and old qNSCs and aNSCs were among the best
685 compared to other cell types (above 0.45). We trained and tested our model performances for 10-

folds; since performance hardly varied across folds, we conducted rest of our analysis on the 1st fold of models. Details of the performances across each sample and each folds, the correlation of the model performances with the imbalance ratio can be found here - http://mitra.stanford.edu/kundaje/msharmin/report/nsc_reports/NSC.html

To identify importance score on the sequences, for each sample we treated the peaks as 1kb sequence centered around the peak summit and interpreted each base using DeepLIFT[35]. DeepLIFT assigns a score for each base of the sequence learned from the model based on how important that base would be with respect to a set of background sequences. Next, we take the importance score tracks and learned the over-represented important sequence patterns using MoDISco[36,37]. MoDISco takes the importance scores, identifies the high scoring sub-sequences (called seqlets) and cluster the seqlets into over-represented patterns called MoDISco-patterns. Notably, given that deep learning models do not give 100% accuracy, we tried to pick the true-positive peaks for finding MoDISco patterns. To clarify further, we interpreted only the peaks, i.e. knowing that peaks are positive examples for the model. Hence, to pass the importance scores to MoDISco, we filtered the peaks with high-scores as positive by the deep learning model. The high-score is defined by the calibrated model-score ([https://github.com/kundajelab/abstention]) which gives 50% FDR cut off for the model performance. Each MoDISco pattern for each sample is then matched with CISBP 2.00 motif database and the matched motifs are listed into separate html files per sample (and per set of differential regions) linked from here (http://mitra.stanford.edu/kundaje/msharmin/report/nsc_reports/NSC.html).

For finding MoDISco pattern in the differential regions we took the previously selected regions (as obtained using DiffBind[89,90]) and retained the regions with 50% overlap with one of the

709 defined 1kb peaks as described above. Then we filtered the differential peak sets based on true-
710 positive peak sets called by the model and used their importance scores on TF-MoDISco to find
711 the set of differential MoDISco patterns.
712
713 **Single cell RNA-seq expression values for Cell Adhesion genes**
714 Single cell gene expression data of the SVZ[25] consisting of 14,685 cells (8,884 cells from young
715 and 5,801 cells from old) were used in order to identify how gene expression differs by cell type
716 and age at single-cell resolution using an orthogonal dataset.
717 Single cell gene expression values for qNSCs/astrocytes, aNSCs/NPCs, and neuroblasts were
718 extracted and subset based on genes from the "Cell Adhesion" GO gene list (GO:0007155). For
719 each single cell within a cell population, the expression levels of cell adhesion genes were
720 summed. The cumulative expression level of adhesion genes comparing young
721 qNSCs/astrocytes, aNSCs/NPCs, and neuroblasts was visualized using violin plots with R
722 (v3.5.2). The cumulative expression level of adhesion genes comparing young and old
723 qNSCs/astrocytes, and young and old aNSCs/NPCs was visualized using violin plots with R
724 (v3.5.2). Statistical comparisons between conditions was performed in R using a two-tailed
725 Mann-Whitney test.
726 Using the same dataset, we investigated the relationship between cell cycle phase and cellular
727 adhesion. To this end, t-SNE analysis was performed on SVZ cells as previously described[25]
728 using the Seurat package (v3.1.5)[100]. The 8,884 single cells from the young SVZ were colored
729 based on expression of genes from the "Cell Adhesion" GO gene list (GO:0007155) as well as
730 by their cell cycle phase for side-by-side comparison.
731

We plotted the relationship between Seurat's "S phase score" and the cumulative expression of genes from the "Cell Adhesion" GO gene list (GO:0007155) in qNSCs/astrocytes, aNSCs/NPCs, and neuroblasts, and found no evidence of a correlative relationship between cellular adhesion and proliferative propensity. For this analysis, each cell population was downsampled to the number of old cells (480 qNSCs/astrocytes, 82 aNSCs/NPCs, and 146 neuroblasts).

Ingenuity Pathway Analysis (IPA)

Genes associated with differentially accessible peaks (FDR<0.05) that open in old aNSCs freshly isolated from the SVZ were uploaded to Ingenuity Pathway Analysis (IPA) (v1.16)[101] (QIAGEN Inc., https://www.qiagenbioinformatics.com/products/ingenuitypathway-analysis) to identify age-related regulatory changes (see Supplementary Table 8). For each peak-associated gene, we uploaded the log fold-change, p-value, and FDR (q-value) and based the IPA analysis on FDR. Statistical enrichment of pathways was reported with *P*-values calculated by IPA using Fisher's Exact Test.

Migration assay of cultured qNSCs and aNSCs/NPCs using live cell imaging

aNSCs/NPCs were cultured in complete activated media until Passage 2-4 and then seeded at a density of 200,000 cells per well in a PDL-coated 12-well plate with complete activated media treated with vehicle (H_2O) or 10μM Y-27632 (dissolved in H_2O) (Tocris, 1254). After 48 hours, adherent aNSCs/NPCs were passaged with 500 μL of Accutase (STEMCELL Technologies, 07920), and resuspended in in Neurobasal-A (Gibco, 10888-022) supplemented with 2% B27 minus vitamin A (Gibco, 12587-010) and 1% penicillin–streptomycin–glutamine (Gibco, 10378-016) with propidium iodide (BioLegend, 421301, 1:5000) for live/dead staining. 1000 live (PI-)

cells per well were sorted with flow cytometry using the BD PICI onto PDL-coated Incucyte ImageLock 96-well plates (Essen BioScience, 4379) containing 100 µL of complete activated media with 10 nM Syto64 (Invitrogen, S11346, Lot #8344573) and either vehicle (H_2O) or 10µM Y-27632 (dissolved in H_2O) (Tocris, 1254). The ImageLock plate was immediately brought to the Incucyte Zoom or Incucyte S3 live imaging system to image (with Phase and RFP channels) at 37°C every 30 min for 20 hours with the 20X objective. After 20 hours, the cell media was washed 2x with PBS and then replaced with 100 µL of complete quiescent media. Media was changed every other day for 7 days to induce quiescence. The media was then replaced with complete quiescent media supplemented with 10 nM Syto64 (Invitrogen, S11346, Lot #8344573) prior to imaging. Wells were imaged (with Phase and RFP channels) using either the Incucyte S3 or Incucyte Zoom system with the 20X objective every hour for 20 hours at 37°C. Three images (from different parts of the well) at each timepoint were taken for each well and tracked cell metrics were summed across these three images. Cell migration tracking was performed using Imaris (v9.3.0). Every image stack was manually curated to ensure that cell tracking was correctly performed (e.g. that automated cell tracking was not incorrectly labelling debris and that cell tracks accurately follow individual cells). "Track Velocity" was output for visualization with Prism (v8) and *P*-values were calculated with a two-tailed Mann-Whitney test comparing both single cell values as well as sample mean values (where single cell velocities are averaged by animal).

Matrigel migration assay

Activated NSCs/NPCs were cultured in complete activated media until Passage 4-6, passaged with Accutase (STEMCELL Technologies, 07920), and resuspended in complete activated

778 media at a concentration of 100,000 cells/μL. Matrigel (Corning, 354230, Lot #8344573) was
779 diluted 1:2 in cold F12:DMEM (Gibco, 11-330-057) while on ice to prevent solidification, and
780 50 μL was immediately added per well to a 96-well plate. The 96-well plate was moved to the
781 37°C incubator for 3 hours prior to spotting 50,000 cells (in a volume of 0.5 μL) directly to the
782 center of the Matrigel-coated well. The plate was returned to the 37°C incubator for 15-30 min to
783 allow for cells to adhere. 150 μL of complete activated media (treated with vehicle (H_2O) or
784 10μM Y-27632 (dissolved in H_2O) (Tocris, 1254)) was very carefully added to each well, and
785 the 96-well plate was placed in either the Incucyte Zoom or Incucyte S3 live imaging system to
786 image every 6 hours for 48 hours using the 4x objective to image the entire well. For each
787 biological replicate, 1-4 technical replicates were quantified to account for difficulties in spotting
788 0.5 μL volumes, and the distances migrated at each timepoint were averaged among technical
789 replicates. We manually quantified invasion distance, defined as the maximum distance from the
790 initial spotting perimeter to the outermost cell body, using Fiji (v2)[102]. Neither imaging nor
791 analysis was performed in a blinded manner. *P*-values were calculated with a two-tailed Mann-
792 Whitney test at each 12-hour timepoint.
793
794 **Immunofluorescence staining of SVZ coronal sections**
795 Four young (4 months old) and four old (18-26 months old) GFAP-GFP animals of both sexes (2
796 male and 2 female animals per age condition) were subjected to intracardiac perfusion with 4%
797 paraformaldehyde (Electron Microscopy Sciences, 15714) in PBS. Brains were post-fixed
798 overnight in 4% paraformaldehyde (Electron Microscopy Sciences, 15714) and then dehydrated
799 in 30% sucrose (Sigma-Aldrich, S3929) for 72 hours. Brains were embedded in Tissue-Tek
800 optimal cutting temperature (O.C.T.) compound (Electron Microscopy Sciences, 62550),

sectioned in 16 μm coronal slices using a cryostat (Leica CM3050S), and then mounted on glass slides (Fisher Scientific, 12-550-15). To ensure a similar anatomic region of the lateral ventricle was being analyzed in each animal, the corpus callosum was first identified in the sections. This section was selected to be stained for cell markers. Two additional sections, approximately 100 μm and 200 μm anterior to the corpus callosum were also selected to be stained for cell markers for a total of 3 sections per animal. To perform immunofluorescent staining, sections were washed with PBS and then permeabilized with ice-cold methanol + 0.1% Triton X-100 (Fisher Scientific, BP151) for 15 min. Slides were washed 3x with PBS for 5 min. Antigen retrieval was performed in 10mM sodium citrate buffer (pH 6.0) (2.94 g Tri-sodium citrate dihydrate (Sigma-Aldrich, S1804) in 1000 mL milliQ H_2O adjusted to pH 6.0 with 1N HCl) + 0.05% TWEEN 20 (Sigma-Aldrich, P1379-1L) at 85°C for 2 hours. Slides were then cooled to room temperature for 20 min, and sections were blocked with 5% Normal Donkey Serum (NDS) (ImmunoReagents Inc., SP-072-VX10) and 1% BSA (Sigma, A7979) in PBS for 30 min at room temperature. Primary antibody staining was performed overnight at 4°C in 5% Normal Donkey Serum and 1% BSA in PBS. Primary antibodies used were the following: Ki67 (Invitrogen, SolA15 [1:200]) and GFAP (Abcam, ab53554, [1:500]). Sections were then washed 3x with PBS and 0.2% TWEEN 20 for 10 min at room temperature followed by two PBS washes for 15 min. Secondary antibody staining was performed at room temperature for 2 hours in 5% NDS and 1% BSA in PBS. Secondary antibodies used were the following: Donkey anti-Goat 488 (Sigma Aldrich, SAB460032-250UL [1:1000]), and Donkey anti-Rat 594 (Life Technologies, A21209 [1:1000]). DAPI (ThermoFisher, 62248 [1:500]) was added during secondary antibody staining. Sections were washed 3x for with PBS and 0.2% TWEEN 20 for 10 min at room temperature followed by 3 PBS washes for 5 min. Sections were mounted with ProLong Gold Antifade Mountant with

824 DAPI (ThermoFisher, P36931) and visualized with a Nikon Eclipse Ti confocal microscope
825 equipped with a Zyla sCMOS camera (Andor) and NIS- Elements software (AR 4.30.02, 64-bit).
826 Multiple Z-stacks using the 60x objective were captured to image the entire length of the SVZ
827 from one hemisphere per section. These Z-stacks (30 slices per stack) were transformed into a Z-
828 projection (max intensity) and quantified using a custom pipeline. GFAP-positive and Ki67-
829 positive nuclei were identified as aNSCs. GFAP-positive and Ki67-negative nuclei were
830 identified as qNSCs/astrocytes. Although rare, NSCs lining blood vessels were censored in the
831 analysis. The center of each NSC nuclei was chosen as a reliable and consistent fixed point to
832 assess cell localization. Distances from the ventricle were calculated by measuring Euclidean
833 distance from the center of the nucleus of each cell of interest to the ventricle border in Fiji (v2).
834 Neither imaging nor analysis was performed in a blinded manner. *P*-values were calculated with
835 a two-tailed Mann-Whitney test. For immunofluorescent images in this manuscript, brightness
836 and contrast were adjusted in Fiji (v2) to enhance visualization. These adjustments were
837 performed after all data quantification was complete. The same settings were applied to all
838 images shown for each experiment.
839
840 ***In vivo* SVZ migration by EdU-labelling**
841 Young (2-3 months) and old (21 months) male C57BL/6 animals were intraperitoneally injected
842 with 5-ethynyl-2'-deoxyuridine (EdU) (Fisher Scientific, A10044) (resuspended in PBS at 5
843 mg/mL) at a dose of 50 mg/kg either 4 hours, 2 days, or 7 days prior to intracardiac perfusion
844 with 4% paraformaldehyde (PFA) (Electron Microscopy Sciences, 15714) in PBS. Brains were
845 post-fixed overnight in 4% PFA and then dehydrated in 30% sucrose (Sigma-Aldrich, S3929) for
846 72 hours. Brains were embedded in Tissue-Tek optimal cutting temperature (O.C.T.) compound

(Electron Microscopy Sciences, 62550) and sectioned in 16 μm sagittal slices using a cryostat (Leica CM3050S) that were then mounted on glass slides (Fisher Scientific, 12-550-15). Immunofluorescent staining of sagittal sections was performed as above (see *Immunofluorescence staining of SVZ coronal sections*) except that the CliCK-IT EdU Alexa Fluor 488 imaging protocol (Thermo Fisher Scientific, C10337) was performed for 30 min at room temperature prior to blocking. The following primary antibodies were used: Ki67 (Invitrogen, SolA15 [1:200]) and DCX (Cell Signaling Technologies, 4604 [1:500]). The following secondary antibodies were used: Donkey anti-Rabbit Alexa 568 (Invitrogen, A10042 [1:500]) and Goat anti-Rat Alexa 647 (Invitrogen, A21247 [1:500]). DAPI (1 mg/mL) (ThermoFisher, 62248) was included at a concentration of 1:500 with the secondary antibody mix. Sections were mounted with ProLong Gold Antifade Mountant with DAPI (ThermoFisher, P36931) and visualized with a Zeiss LSM 900 confocal microscope equipped with Zeiss ZEN Blue 3.0 software.

Multiple sections per brain were stained and imaged to determine the optimal depth to capture SVZ/RMS migration and the most appropriate section per animal was imaged and quantified. Appropriate sections were selected based on presence of an intact RMS as judged by a stream of DCX-positive cells connecting the SVZ to the OB. Images of sagittal sections were captured using a 5x objective and 9x3 images (for a total of 27) were automatically stitched together using the Zeiss ZEN Blue 3.0 software. For quantification, EdU-labelled nuclei were counted using Fiji (v2)[102]. Briefly, every image was converted to 8-bit, the threshold was adjusted ((90,255) for replicate 1 and (70,255) for replicate 2), watershed was applied to the image and EdU-labelled nuclei were counted with "Analyze Particles (size (micron^2): (20-infinity) for replicate 1 and 2, and circularity: (0.2-1.00) for replicate 1)". EdU-labelled nuclei were quantified in three regions

(SVZ, RMS, and OB) which were manually defined using a hand-drawn region of interest (ROI) for each slide. To calculate distances of EdU+ cells from the ventricle, images of the SVZ from the sagittal sections used above were captured using a 20x objective and subject to the same analysis as described in (*Immunofluorescence staining of SVZ coronal sections)*. EdU+ cells were classified as aNSCs/NPCs if they were Ki67-positive and DCX-negative and as neuroblasts if they were DCX-positive. One old 7-day post-injection replicate from the first experiment was censored due to a failed intraperitoneal EdU injection and one young 7-day post-injection replicate from the second experiment was censored due to lack of high quality sections at the appropriate depth. Neither imaging nor analysis was performed in a blinded manner. *P*-values were calculated with a two-tailed Mann-Whitney test.

Immunofluorescence staining of young and old cultured NSCs

NSCs were cultured as described above (see *Primary NSC culture*) in complete activated media until Passage 2-3 and then seeded at a density of 200,000 cells per well in a PDL-coated 12-well plate with complete activated media. After 48 hours, adherent aNSCs/NPCs were passaged with 500 µL of Accutase (STEMCELL Technologies, 07920), and resuspended in Neurobasal-A (Gibco, 10888-022) supplemented with 2% B27 minus vitamin A (Gibco, 12587-010) and 1% penicillin–streptomycin–glutamine (Gibco, 10378-016) with propidium iodide (BioLegend, 421301, 1:5000) for live/dead staining. 1000 live (PI-) cells per well were FACS sorted using the BD PICI onto PDL-coated glass-bottomed 96-well plates (Cellvis, P96-1.5H-N) containing 100 µL of either complete activated media or complete quiescent media. After 24 hours for the activated plates and 5-7 days for the quiescent plates, the sorted wells were washed 1x with PBS, then fixed with 4% paraformaldehyde (Electron Microscopy Sciences, 15714) for 15 min. Wells

were washed 4x with PBS and then stored, wrapped in parafilm, at 4°C until immunofluorescence staining. Cells were washed 2x with PBS and permeabilized with 0.1% Triton X-100 (Fisher Scientific, BP151). Blocking was performed for 30 min with 1% BSA (Sigma, A7979) in PBS. Primary staining was conducted for 1 hour at room temperature with phalloidin (Invitrogen, A12379, 665217, 1:500) resuspended in 1% BSA (Sigma, A7979). Wells were then washed 4x with PBS and secondary staining was performed for 1 hour at room temperature with Donkey anti-Rabbit Alexa 568 (Invitrogen, A10042, 1:500) resuspended in 1% BSA (Sigma, A7979). Wells were washed 4x with PBS+0.2% TWEEN 20 (Sigma-Aldrich, P1379-1L), then 4x with PBS prior to imaging. Imaging was performed on a Nikon Eclipse Ti confocal microscope equipped with a Zyla sCMOS camera (Andor) and NIS- Elements software (AR 4.30.02, 64-bit) using the 60x objective. Quantification of immunofluorescence staining of F-actin was done using a custom pipeline in Fiji (v2)[102]. Fluorescence intensity in regions of high-density phalloidin staining were quantified as a proxy for bundled actin. Briefly, images were converted to 8-bit, inverted and an intensity threshold was manually set in the phalloidin channel to generate a mask. The same threshold values were used for all images across all conditions in each individual experiment. The sum of pixel intensity within the cell mask (RawIntDen) was then used to determine fluorescence intensity for each cell. For each experiment, values were normalized by dividing each cell's fluorescence intensity by the mean fluorescence intensity of all cells in the young condition. Neither imaging nor analysis was performed in a blinded manner. *P*-values were calculated with a two-tailed Mann-Whitney test.

RGD molecular tension sensor FRET measurements of cultured NSCs

Sensors containing a minimal RGD sequence derived from fibronectin

916 (TVYAVTGRGDSPASSAA) were expressed, purified, and labeled with AlexaFluor-546 and -
917 647, and coverslips passivated with maleimide polyethylene glycol (PEG) succinimidyl
918 carboxymethyl ester (JenKem Technology, A5003-1) were prepared as previously
919 described[55,103]. Flow chambers for imaging were prepared as described[103] with slight
920 modifications. 8-well flow chambers (Grace BioLabs, #622505, ~55µL channel volume) were
921 attached to PEGylated coverslips as previously described[104]. Chambers were incubated with 300
922 nM double-labeled sensor at room temperature for 45 min. The chambers were then washed with
923 150 µL of PBS for 1 min to prevent non-specific cell attachment. 60 µL of cell suspensions at a
924 density of 300,000-400,000 cells/mL were added to the channels, and the chambers were
925 incubated for 3 hours at 37°C and 5% CO2 in complete activation media to allow cells to spread.
926 Chambers were then washed with 150 µL of warm media, and brightfield and FRET
927 measurements were made immediately after and acquired with an objective heater (Bioptechs)
928 set to 37°C. For measurements on cells treated with Y-27632, complete activation media was
929 supplemented with 10µM Y-27632 (dissolved in H_2O) (Tocris, 1254)) for cell suspensions and
930 media washes.
931 We limited our measurements and analysis to individual cells that looked well-spread in
932 brightfield and cell clusters of no more than 5 cells in which cell outlines could be clearly
933 distinguished. FRET fluorescence measurements were performed with objective-type total
934 internal reflection fluorescence (TIRF) microscopy on an inverted microscope (Nikon TiE) with
935 an Apo TIRF 100× oil objective lens, numerical aperture 1.49 (Nikon) as described previously[55]
936 and controlled using Micromanager[105]. Samples were excited with 532-nm (Crystalaser) or 635-
937 nm (Blue Sky Research) lasers. Emitted light passed through a quad-edge laser-flat dichroic with
938 center/bandwidths of 405/60 nm, 488/100 nm, 532/100 nm, and 635/100 nm from Semrock Inc.

(Di01-R405/488/532/635-25×36) and corresponding quad-pass filter with center/bandwidths of 446/37 nm, 510/20 nm, 581/70 nm, 703/88 nm band-pass filter (FF01-446/510/581/703-25). Donor and acceptor images were taken through separate additional cubes stacked into the light path (donor: 550 nm long-pass; acceptor: 679/41 nm and 700/75 nm) and recorded on a Hamamatsu Orca Flash 4.0 camera.

Images were prepared in Fiji (v2)[102] and analyzed using custom MATLAB scripts, in which FRET efficiencies were computed and thresholded to identify adhesions and quantify forces within adhesions. An appreciable fraction of cultured aNSCs/NPCs seeded on RGD molecular tension sensors did not exhibit distinct focal adhesion patterns upon analysis, potentially reflecting cells generating tractions below the sensitivity threshold of the assay. To compare the adhesive forces of these cells with those that had distinct focal adhesions, we used the average FRET/force values underneath the entire cell body as a metric for the adhesive strength in cells without adhesions. While we observed significant differences in fractions of old and young aNSCs exhibiting force-generating adhesions through this analysis, we observed that these differences may be driven by divergent phenotypes in integrin-mediated force upon contact with other cells. For the cells that were imaged and analyzed, we observed little difference in focal adhesion phenotype in isolated cells but sharp differences in phenotype in cells that were in small clusters. These data are aggregated in Fig. 4e,f, Fig. 5d,e, and Extended Fig. 8.

Immunofluorescence staining of cultured NSCs treated with ROCK inhibition

aNSCs/NPCs were cultured as described above (see *Primary NSC culture*) in complete activated media until Passage 2-3 and then seeded at a density of 200,000 cells per well in a PDL-coated 12-well plate with complete activated media treated with vehicle (H_2O) or 10μM Y-27632

(dissolved in H_2O) (Tocris, 1254). After 48 hours, adherent aNSCs/NPCs were passaged with 500 µL of Accutase (STEMCELL Technologies, 07920), and resuspended in Neurobasal-A (Gibco, 10888-022) supplemented with 2% B27 minus vitamin A (Gibco, 12587-010) and 1% penicillin–streptomycin–glutamine (Gibco, 10378-016) with propidium iodide (BioLegend, 421301, 1:5000) for live/dead staining. 1000 live (PI-) cells per well were FACS sorted using the BD PICI onto PDL-coated glass-bottomed 96-well plates (Cellvis, P96-1.5H-N) containing 100 µL of complete activated media treated with vehicle (H_2O) or 10µM Y-27632 (dissolved in H_2O) (Tocris, 1254). After 24 hours, the sorted wells were washed 1x with PBS, then fixed with 4% paraformaldehyde (Electron Microscopy Sciences, 15714) for 15 min. Wells were washed 4x with PBS and then stored, wrapped in parafilm, at 4°C until immunofluorescence staining. Staining and quantification of old cultured aNSCs/NPCs for ROCK inhibition experiments was otherwise performed in the same manner as described above (see *Immunofluorescence staining of young and old cultured NSCs*).

Statistical analyses

For all experiments, young and old conditions were processed in an alternate manner rather than in two large groups, to minimize the group effect. We did not perform power analyses, though we did take into account previous experiments to determine the number of animals needed. To calculate statistical significance for experiments, all tests were two-sided Mann-Whitney tests (with the exception of Fisher's Exact Tests which are noted in Figure Legends). Results from individual experiments and all statistical analyses are included in Supplementary Table 1.

References

1. Bond, A.M., Ming, G.L. & Song, H. Adult Mammalian Neural Stem Cells and Neurogenesis: Five Decades Later. *Cell Stem Cell* **17**, 385-95 (2015).
2. Hattiangady, B., Rao, M.S. & Shetty, A.K. Plasticity of hippocampal stem/progenitor cells to enhance neurogenesis in response to kainate-induced injury is lost by middle age. *Aging Cell* **7**, 207-24 (2008).
3. Conover, J.C. & Shook, B.A. Aging of the subventricular zone neural stem cell niche. *Aging Dis* **2**, 49-63 (2011).
4. Navarro Negredo, P., Yeo, R.W. & Brunet, A. Aging and Rejuvenation of Neural Stem Cells and Their Niches. *Cell Stem Cell* **27**, 202-223 (2020).
5. Nicaise, A.M., Willis, C.M., Crocker, S.J. & Pluchino, S. Stem Cells of the Aging Brain. *Front Aging Neurosci* **12**, 247 (2020).
6. Rao, M.S., Hattiangady, B. & Shetty, A.K. Status epilepticus during old age is not associated with enhanced hippocampal neurogenesis. *Hippocampus* **18**, 931-44 (2008).
7. Mirzadeh, Z., Merkle, F.T., Soriano-Navarro, M., Garcia-Verdugo, J.M. & Alvarez-Buylla, A. Neural stem cells confer unique pinwheel architecture to the ventricular surface in neurogenic regions of the adult brain. *Cell Stem Cell* **3**, 265-78 (2008).
8. Shen, Q. *et al.* Adult SVZ stem cells lie in a vascular niche: a quantitative analysis of niche cell-cell interactions. *Cell Stem Cell* **3**, 289-300 (2008).
9. Tavazoie, M. *et al.* A specialized vascular niche for adult neural stem cells. *Cell Stem Cell* **3**, 279-88 (2008).

10. Doetsch, F., Garcia-Verdugo, J.M. & Alvarez-Buylla, A. Cellular composition and three-dimensional organization of the subventricular germinal zone in the adult mammalian brain. *J Neurosci* **17**, 5046-61 (1997).

11. Kernie, S.G. & Parent, J.M. Forebrain neurogenesis after focal Ischemic and traumatic brain injury. *Neurobiol Dis* **37**, 267-74 (2010).

12. Faiz, M. *et al.* Adult Neural Stem Cells from the Subventricular Zone Give Rise to Reactive Astrocytes in the Cortex after Stroke. *Cell Stem Cell* **17**, 624-34 (2015).

13. Capilla-Gonzalez, V., Cebrian-Silla, A., Guerrero-Cazares, H., Garcia-Verdugo, J.M. & Quinones-Hinojosa, A. Age-related changes in astrocytic and ependymal cells of the subventricular zone. *Glia* **62**, 790-803 (2014).

14. Enwere, E. *et al.* Aging results in reduced epidermal growth factor receptor signaling, diminished olfactory neurogenesis, and deficits in fine olfactory discrimination. *J Neurosci* **24**, 8354-65 (2004).

15. Luo, J., Daniels, S.B., Lennington, J.B., Notti, R.Q. & Conover, J.C. The aging neurogenic subventricular zone. *Aging Cell* **5**, 139-52 (2006).

16. Tropepe, V., Craig, C.G., Morshead, C.M. & van der Kooy, D. Transforming growth factor-alpha null and senescent mice show decreased neural progenitor cell proliferation in the forebrain subependyma. *J Neurosci* **17**, 7850-9 (1997).

17. Klemm, S.L., Shipony, Z. & Greenleaf, W.J. Chromatin accessibility and the regulatory epigenome. *Nat Rev Genet* **20**, 207-220 (2019).

18. Kane, A.E. & Sinclair, D.A. Epigenetic changes during aging and their reprogramming potential. *Crit Rev Biochem Mol Biol* **54**, 61-83 (2019).

19. Gontier, G. *et al.* Tet2 Rescues Age-Related Regenerative Decline and Enhances Cognitive Function in the Adult Mouse Brain. *Cell Rep* **22**, 1974-1981 (2018).

20. Martynoga, B. *et al.* Epigenomic enhancer annotation reveals a key role for NFIX in neural stem cell quiescence. *Genes Dev* **27**, 1769-86 (2013).

21. Lupo, G. *et al.* Molecular profiling of aged neural progenitors identifies Dbx2 as a candidate regulator of age-associated neurogenic decline. *Aging Cell* **17**, e12745 (2018).

22. Benayoun, B.A. *et al.* Remodeling of epigenome and transcriptome landscapes with aging in mice reveals widespread induction of inflammatory responses. *Genome Res* **29**, 697-709 (2019).

23. Shi, Z. *et al.* Single-cell transcriptomics reveals gene signatures and alterations associated with aging in distinct neural stem/progenitor cell subpopulations. *Protein Cell* **9**, 351-364 (2018).

24. Artegiani, B. *et al.* A Single-Cell RNA Sequencing Study Reveals Cellular and Molecular Dynamics of the Hippocampal Neurogenic Niche. *Cell Rep* **21**, 3271-3284 (2017).

25. Dulken, B.W. *et al.* Single-cell analysis reveals T cell infiltration in old neurogenic niches. *Nature* **571**, 205-210 (2019).

26. Kalamakis, G. *et al.* Quiescence Modulates Stem Cell Maintenance and Regenerative Capacity in the Aging Brain. *Cell* **176**, 1407-1419 e14 (2019).

27. Codega, P. *et al.* Prospective identification and purification of quiescent adult neural stem cells from their in vivo niche. *Neuron* **82**, 545-59 (2014).

28. Leeman, D.S. *et al.* Lysosome activation clears aggregates and enhances quiescent neural stem cell activation during aging. *Science* **359**, 1277-1283 (2018).

1050 29. Buenrostro, J.D., Giresi, P.G., Zaba, L.C., Chang, H.Y. & Greenleaf, W.J. Transposition
1051 of native chromatin for fast and sensitive epigenomic profiling of open chromatin, DNA-
1052 binding proteins and nucleosome position. *Nat Methods* **10**, 1213-8 (2013).
1053 30. Ucar, D. *et al.* The chromatin accessibility signature of human immune aging stems from
1054 CD8(+) T cells. *J Exp Med* **214**, 3123-3144 (2017).
1055 31. Shcherbina, A. *et al.* Dissecting Murine Muscle Stem Cell Aging through Regeneration
1056 Using Integrative Genomic Analysis. *Cell Rep* **32**, 107964 (2020).
1057 32. Koohy, H. *et al.* Genome organization and chromatin analysis identify transcriptional
1058 downregulation of insulin-like growth factor signaling as a hallmark of aging in
1059 developing B cells. *Genome Biol* **19**, 126 (2018).
1060 33. Ge, Y. *et al.* The aging skin microenvironment dictates stem cell behavior. *Proc Natl*
1061 *Acad Sci U S A* **117**, 5339-5350 (2020).
1062 34. Guillemot, F. & Hassan, B.A. Beyond proneural: emerging functions and regulations of
1063 proneural proteins. *Curr Opin Neurobiol* **42**, 93-101 (2017).
1064 35. Shrikumar, A., Greenside, P. & Kundaje, A. Learning Important Features Through
1065 Propagating Activation Differences. in *Proceedings of the 34th International Conference*
1066 *on Machine Learning* Vol. 70 (eds Doina, P. & Yee Whye, T.) 3145--3153 (PMLR,
1067 Proceedings of Machine Learning Research, 2017).
1068 36. Avsec, Z. *et al.* Base-resolution models of transcription-factor binding reveal soft motif
1069 syntax. *Nat Genet* **53**, 354-366 (2021).
1070 37. Shrikumar, A. *et al.* Technical Note on Transcription Factor Motif Discovery from
1071 Importance Scores (TF-MoDISco) version 0.5.6.5. arXiv:1811.00416 (2018).

1072 38. Fane, M., Harris, L., Smith, A.G. & Piper, M. Nuclear factor one transcription factors as
1073 epigenetic regulators in cancer. *Int J Cancer* **140**, 2634-2641 (2017).
1074 39. Mira, H. *et al.* Signaling through BMPR-IA regulates quiescence and long-term activity
1075 of neural stem cells in the adult hippocampus. *Cell Stem Cell* **7**, 78-89 (2010).
1076 40. Jones, K.M. *et al.* CHD7 maintains neural stem cell quiescence and prevents premature
1077 stem cell depletion in the adult hippocampus. *Stem Cells* **33**, 196-210 (2015).
1078 41. Knobloch, M. *et al.* A Fatty Acid Oxidation-Dependent Metabolic Shift Regulates Adult
1079 Neural Stem Cell Activity. *Cell Rep* **20**, 2144-2155 (2017).
1080 42. Mizrahi, A., Lu, J., Irving, R., Feng, G. & Katz, L.C. In vivo imaging of juxtaglomerular
1081 neuron turnover in the mouse olfactory bulb. *Proc Natl Acad Sci U S A* **103**, 1912-7
1082 (2006).
1083 43. Gage, F.H. & Temple, S. Neural stem cells: generating and regenerating the brain.
1084 *Neuron* **80**, 588-601 (2013).
1085 44. Mobley, A.S. *et al.* Age-dependent regional changes in the rostral migratory stream.
1086 *Neurobiol Aging* **34**, 1873-81 (2013).
1087 45. Shuboni-Mulligan, D.D. *et al.* In vivo serial MRI of age-dependent neural progenitor cell
1088 migration in the rat brain. *Neuroimage* **199**, 153-159 (2019).
1089 46. Capilla-Gonzalez, V., Cebrian-Silla, A., Guerrero-Cazares, H., Garcia-Verdugo, J.M. &
1090 Quinones-Hinojosa, A. The generation of oligodendroglial cells is preserved in the rostral
1091 migratory stream during aging. *Front Cell Neurosci* **7**, 147 (2013).
1092 47. Fritze, J. *et al.* Loss of Cxcr5 alters neuroblast proliferation and migration in the aged
1093 brain. *Stem Cells* **38**, 1175-1187 (2020).

1094 48. Morante-Redolat, J.M. & Porlan, E. Neural Stem Cell Regulation by Adhesion Molecules
1095 Within the Subependymal Niche. *Front Cell Dev Biol* **7**, 102 (2019).
1096 49. Tario, J.D., Jr., Conway, A.N., Muirhead, K.A. & Wallace, P.K. Monitoring Cell
1097 Proliferation by Dye Dilution: Considerations for Probe Selection. *Methods Mol Biol*
1098 **1678**, 249-299 (2018).
1099 50. Molofsky, A.V. *et al.* Increasing p16INK4a expression decreases forebrain progenitors
1100 and neurogenesis during ageing. *Nature* **443**, 448-52 (2006).
1101 51. Ahlenius, H., Visan, V., Kokaia, M., Lindvall, O. & Kokaia, Z. Neural stem and
1102 progenitor cells retain their potential for proliferation and differentiation into functional
1103 neurons despite lower number in aged brain. *J Neurosci* **29**, 4408-19 (2009).
1104 52. Blanchoin, L., Boujemaa-Paterski, R., Sykes, C. & Plastino, J. Actin dynamics,
1105 architecture, and mechanics in cell motility. *Physiol Rev* **94**, 235-63 (2014).
1106 53. Thomas, C. Bundling actin filaments from membranes: some novel players. *Front Plant*
1107 *Sci* **3**, 188 (2012).
1108 54. Morimatsu, M., Mekhdjian, A.H., Adhikari, A.S. & Dunn, A.R. Molecular tension
1109 sensors report forces generated by single integrin molecules in living cells. *Nano Lett* **13**,
1110 3985-9 (2013).
1111 55. Chang, A.C. *et al.* Single Molecule Force Measurements in Living Cells Reveal a
1112 Minimally Tensioned Integrin State. *ACS Nano* **10**, 10745-10752 (2016).
1113 56. Suzuki, N., Hajicek, N. & Kozasa, T. Regulation and physiological functions of G12/13-
1114 mediated signaling pathways. *Neurosignals* **17**, 55-70 (2009).
1115 57. Amano, M., Nakayama, M. & Kaibuchi, K. Rho-kinase/ROCK: A key regulator of the
1116 cytoskeleton and cell polarity. *Cytoskeleton (Hoboken)* **67**, 545-54 (2010).

58. Burridge, K. & Wennerberg, K. Rho and Rac take center stage. *Cell* **116**, 167-79 (2004).

59. Christie, K.J., Turbic, A. & Turnley, A.M. Adult hippocampal neurogenesis, Rho kinase inhibition and enhancement of neuronal survival. *Neuroscience* **247**, 75-83 (2013).

60. Emre, N. *et al.* The ROCK inhibitor Y-27632 improves recovery of human embryonic stem cells after fluorescence-activated cell sorting with multiple cell surface markers. *PLoS One* **5**, e12148 (2010).

61. Ishizaki, T. *et al.* Pharmacological properties of Y-27632, a specific inhibitor of rho-associated kinases. *Mol Pharmacol* **57**, 976-83 (2000).

62. Uehata, M. *et al.* Calcium sensitization of smooth muscle mediated by a Rho-associated protein kinase in hypertension. *Nature* **389**, 990-4 (1997).

63. Kim, J.E., Ryu, H.J., Kim, M.J. & Kang, T.C. LIM kinase-2 induces programmed necrotic neuronal death via dysfunction of DRP1-mediated mitochondrial fission. *Cell Death Differ* **21**, 1036-49 (2014).

64. Leong, S.Y., Faux, C.H., Turbic, A., Dixon, K.J. & Turnley, A.M. The Rho kinase pathway regulates mouse adult neural precursor cell migration. *Stem Cells* **29**, 332-43 (2011).

65. Peh, G.S. *et al.* The effects of Rho-associated kinase inhibitor Y-27632 on primary human corneal endothelial cells propagated using a dual media approach. *Sci Rep* **5**, 9167 (2015).

66. Narumiya, S., Ishizaki, T. & Uehata, M. Use and properties of ROCK-specific inhibitor Y-27632. *Methods Enzymol* **325**, 273-84 (2000).

67. Tumpel, S. & Rudolph, K.L. Quiescence: Good and Bad of Stem Cell Aging. *Trends Cell Biol* **29**, 672-685 (2019).

1140 68. Liu, L. *et al.* Chromatin modifications as determinants of muscle stem cell quiescence
1141 and chronological aging. *Cell Rep* **4**, 189-204 (2013).
1142 69. Schworer, S. *et al.* Epigenetic stress responses induce muscle stem-cell ageing by Hoxa9
1143 developmental signals. *Nature* **540**, 428-432 (2016).
1144 70. Sun, D. *et al.* Epigenomic profiling of young and aged HSCs reveals concerted changes
1145 during aging that reinforce self-renewal. *Cell Stem Cell* **14**, 673-88 (2014).
1146 71. Bock, C. *et al.* DNA methylation dynamics during in vivo differentiation of blood and
1147 skin stem cells. *Mol Cell* **47**, 633-47 (2012).
1148 72. Beerman, I. *et al.* Proliferation-dependent alterations of the DNA methylation landscape
1149 underlie hematopoietic stem cell aging. *Cell Stem Cell* **12**, 413-25 (2013).
1150 73. Mauffrey, P. *et al.* Progenitors from the central nervous system drive neurogenesis in
1151 cancer. *Nature* **569**, 672-678 (2019).
1152 74. Miroshnikova, Y.A., Nava, M.M. & Wickstrom, S.A. Emerging roles of mechanical
1153 forces in chromatin regulation. *J Cell Sci* **130**, 2243-2250 (2017).
1154 75. Nava, M.M. *et al.* Heterochromatin-Driven Nuclear Softening Protects the Genome
1155 against Mechanical Stress-Induced Damage. *Cell* **181**, 800-817 e22 (2020).
1156 76. Segel, M. *et al.* Niche stiffness underlies the ageing of central nervous system progenitor
1157 cells. *Nature* **573**, 130-134 (2019).
1158 77. Goetsch, K.P., Snyman, C., Myburgh, K.H. & Niesler, C.U. ROCK-2 is associated with
1159 focal adhesion maturation during myoblast migration. *J Cell Biochem* **115**, 1299-307
1160 (2014).
1161 78. Salhia, B. *et al.* Inhibition of Rho-kinase affects astrocytoma morphology, motility, and
1162 invasion through activation of Rac1. *Cancer Res* **65**, 8792-800 (2005).

1163 79. Chen, Y., Chou, W.C., Ding, Y.M. & Wu, Y.C. Caffeine inhibits migration in glioma
1164 cells through the ROCK-FAK pathway. *Cell Physiol Biochem* **33**, 1888-98 (2014).
1165 80. Fu, P.C. *et al.* The Rho-associated kinase inhibitors Y27632 and fasudil promote
1166 microglial migration in the spinal cord via the ERK signaling pathway. *Neural Regen Res*
1167 **13**, 677-683 (2018).
1168 81. Piltti, J., Varjosalo, M., Qu, C., Hayrinen, J. & Lammi, M.J. Rho-kinase inhibitor Y-
1169 27632 increases cellular proliferation and migration in human foreskin fibroblast cells.
1170 *Proteomics* **15**, 2953-65 (2015).
1171 82. Rudolph, J. *et al.* The JAK inhibitor ruxolitinib impairs dendritic cell migration via off-
1172 target inhibition of ROCK. *Leukemia* **30**, 2119-2123 (2016).
1173 83. Srinivasan, S. *et al.* Blockade of ROCK inhibits migration of human primary
1174 keratinocytes and malignant epithelial skin cells by regulating actomyosin contractility.
1175 *Sci Rep* **9**, 19930 (2019).
1176 84. Dyberg, C. *et al.* Inhibition of Rho-Associated Kinase Suppresses Medulloblastoma
1177 Growth. *Cancers (Basel)* **12**(2019).
1178 85. Feng, J.F. *et al.* Guided migration of neural stem cells derived from human embryonic
1179 stem cells by an electric field. *Stem Cells* **30**, 349-55 (2012).
1180 86. Koch, J.C. *et al.* ROCK inhibition in models of neurodegeneration and its potential for
1181 clinical translation. *Pharmacol Ther* **189**, 1-21 (2018).
1182 87. Zhuo, L. *et al.* Live astrocytes visualized by green fluorescent protein in transgenic mice.
1183 *Dev Biol* **187**, 36-42 (1997).

88. Shen, L., Shao, N., Liu, X. & Nestler, E. ngs.plot: Quick mining and visualization of next-generation sequencing data by integrating genomic databases. *BMC Genomics* **15**, 284 (2014).

89. Stark, R.B., G.D. DiffBind: differential binding analysis of ChIP-seq peak data. *Bioconductor* (2011).

90. Ross-Innes, C.S. *et al.* Differential oestrogen receptor binding is associated with clinical outcome in breast cancer. *Nature* **481**, 389-93 (2012).

91. Yu, G., Wang, L.G. & He, Q.Y. ChIPseeker: an R/Bioconductor package for ChIP peak annotation, comparison and visualization. *Bioinformatics* **31**, 2382-3 (2015).

92. Love, M.I., Huber, W. & Anders, S. Moderated estimation of fold change and dispersion for RNA-seq data with DESeq2. *Genome Biol* **15**, 550 (2014).

93. Robinson, M.D., McCarthy, D.J. & Smyth, G.K. edgeR: a Bioconductor package for differential expression analysis of digital gene expression data. *Bioinformatics* **26**, 139-40 (2010).

94. McCarthy, D.J., Chen, Y. & Smyth, G.K. Differential expression analysis of multifactor RNA-Seq experiments with respect to biological variation. *Nucleic Acids Res* **40**, 4288-97 (2012).

95. Schep, A.N. *et al.* Structured nucleosome fingerprints enable high-resolution mapping of chromatin architecture within regulatory regions. *Genome Res* **25**, 1757-70 (2015).

96. Chen, E.Y. *et al.* Enrichr: interactive and collaborative HTML5 gene list enrichment analysis tool. *BMC Bioinformatics* **14**, 128 (2013).

97. Kuleshov, M.V. *et al.* Enrichr: a comprehensive gene set enrichment analysis web server 2016 update. *Nucleic Acids Res* **44**, W90-7 (2016).

98. Heinz, S. *et al.* Simple combinations of lineage-determining transcription factors prime cis-regulatory elements required for macrophage and B cell identities. *Mol Cell* **38**, 576-89 (2010).

99. Kelley, D.R., Snoek, J. & Rinn, J.L. Basset: learning the regulatory code of the accessible genome with deep convolutional neural networks. *Genome Res* **26**, 990-9 (2016).

100. Stuart, T. *et al.* Comprehensive Integration of Single-Cell Data. *Cell* **177**, 1888-1902 e21 (2019).

101. Kramer, A., Green, J., Pollard, J., Jr. & Tugendreich, S. Causal analysis approaches in Ingenuity Pathway Analysis. *Bioinformatics* **30**, 523-30 (2014).

102. Schindelin, J. *et al.* Fiji: an open-source platform for biological-image analysis. *Nat Methods* **9**, 676-82 (2012).

103. Tan, S.J. *et al.* Regulation and dynamics of force transmission at individual cell-matrix adhesion bonds. *Sci Adv* **6**, eaax0317 (2020).

104. Morimatsu, M., Mekhdjian, A.H., Chang, A.C., Tan, S.J. & Dunn, A.R. Visualizing the interior architecture of focal adhesions with high-resolution traction maps. *Nano Lett* **15**, 2220-8 (2015).

105. Edelstein, A.D. *et al.* Advanced methods of microscope control using muManager software. *J Biol Methods* **1**(2014).

Figure 1

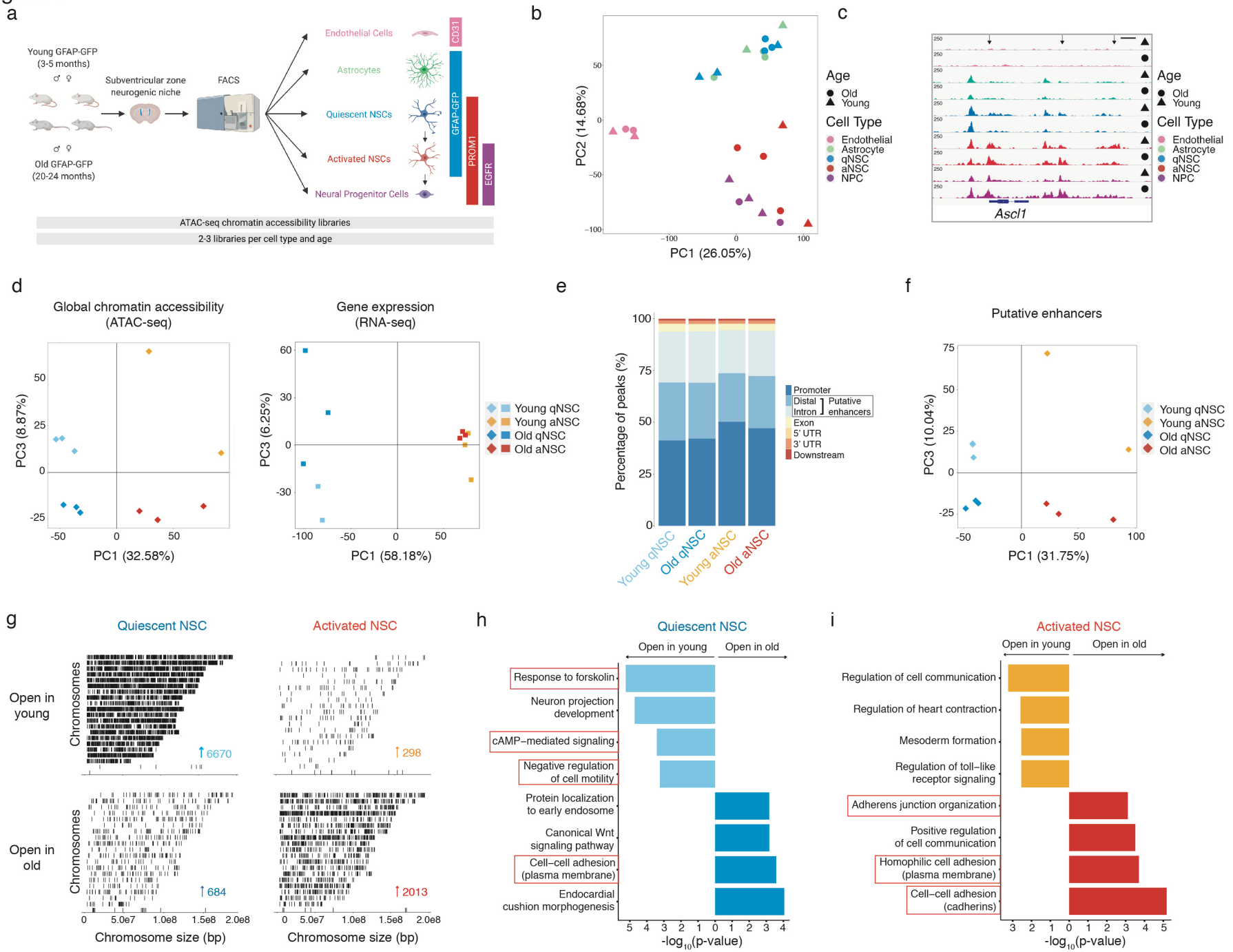

Figure 1: The chromatin landscape of five cell types in the SVZ neurogenic region reveals opposing chromatin changes with age in quiescent and activated NSCs involving cell adhesion and migration pathways

a) Experimental design for freshly isolating cells from the subventricular zone (SVZ) neurogenic niche in young (3-5 months) and old (20-24 months) GFAP-GFP mice. For each library, 800-2000 cells were pooled from male and female GFAP-GFP mice using fluorescence-activated cell sorted (FACS) (see Methods). NSC: neural stem cell. GFAP, Glial Fibrillary Acidic Protein. PROM1, Prominin-1. EGFR, epidermal growth factor receptor.

b) Principal Component Analysis (PCA) on all chromatin peaks from endothelial cells, astrocytes, quiescent NSCs (qNSCs), activated NSCs (aNSCs), and neural progenitor cells (NPCs) freshly isolated from the SVZ of young (triangle) and old (round) GFAP-GFP mice where each dot represents a single ATAC-seq library. PCA was generated using the variance stabilizing transformation (VST)-normalized global consensus count matrix. PC, principal component.

c) Genome browser (IGV) view of chromatin accessibility signal tracks from representative RPKM-normalized libraries of all SVZ niche cell types around the *Ascl1* loci. Black arrows represent sites of differentially accessible peaks that open in young aNSCs when compared to young qNSCs. *Ascl1*, Achaete-Scute Family bHLH Transcription Factor 1. Scale bar, 1kb.

d) PCA on all genome-wide chromatin peaks (left) and mRNA gene expression[28] (right) from qNSCs and aNSCs freshly isolated from the young and old SVZ where each dot represents a single sequencing library (PC1 vs. PC3). ATAC-seq libraries are represented by diamonds

and RNA-seq libraries are represented by squares. PCAs were both generated using variance stabilizing transformation (VST)-normalized read counts. PC, principal component.

e) Bar graph representing the genomic distribution of open chromatin peaks for qNSCs and aNSCs in young and old conditions based on their pooled peaksets. ATAC-seq peaks were annotated with ChIPSeeker (v1.18.0). Grey box indicates distal and intronic peaks that likely contain putative enhancers.

f) PCA on putative enhancers (exclusively distal/intronic chromatin peaks) from qNSCs and aNSCs freshly isolated from the young and old SVZ where each dot represents a single ATAC-seq library (PC1 vs. PC3). PCA was generated using the variance stabilizing transformation (VST)-normalized NSC consensus count matrix. PC, principal component.

g) Chromosome-level visualization of differentially accessible ATAC-seq peaks (FDR<0.05) that change with age in qNSCs (left) and aNSCs (right) respectively. Each vertical bar represents a dynamic ATAC-seq peak aligned to mouse chromosomes (*mm10* version of the mouse genome) that is differentially open in young (top) or old (bottom) NSCs.

h,i) Selected GO terms for genes associated with differentially accessible ATAC-seq peaks (FDR<0.05) that change with age in quiescent (h) and activated (i) NSCs generated by EnrichR and ranked by *P*-value. ATAC-seq peaks were annotated with their nearest gene using ChIPSeeker (v1.18.0). Red boxes indicate GO terms associated with adhesion and migration.

Figure 2

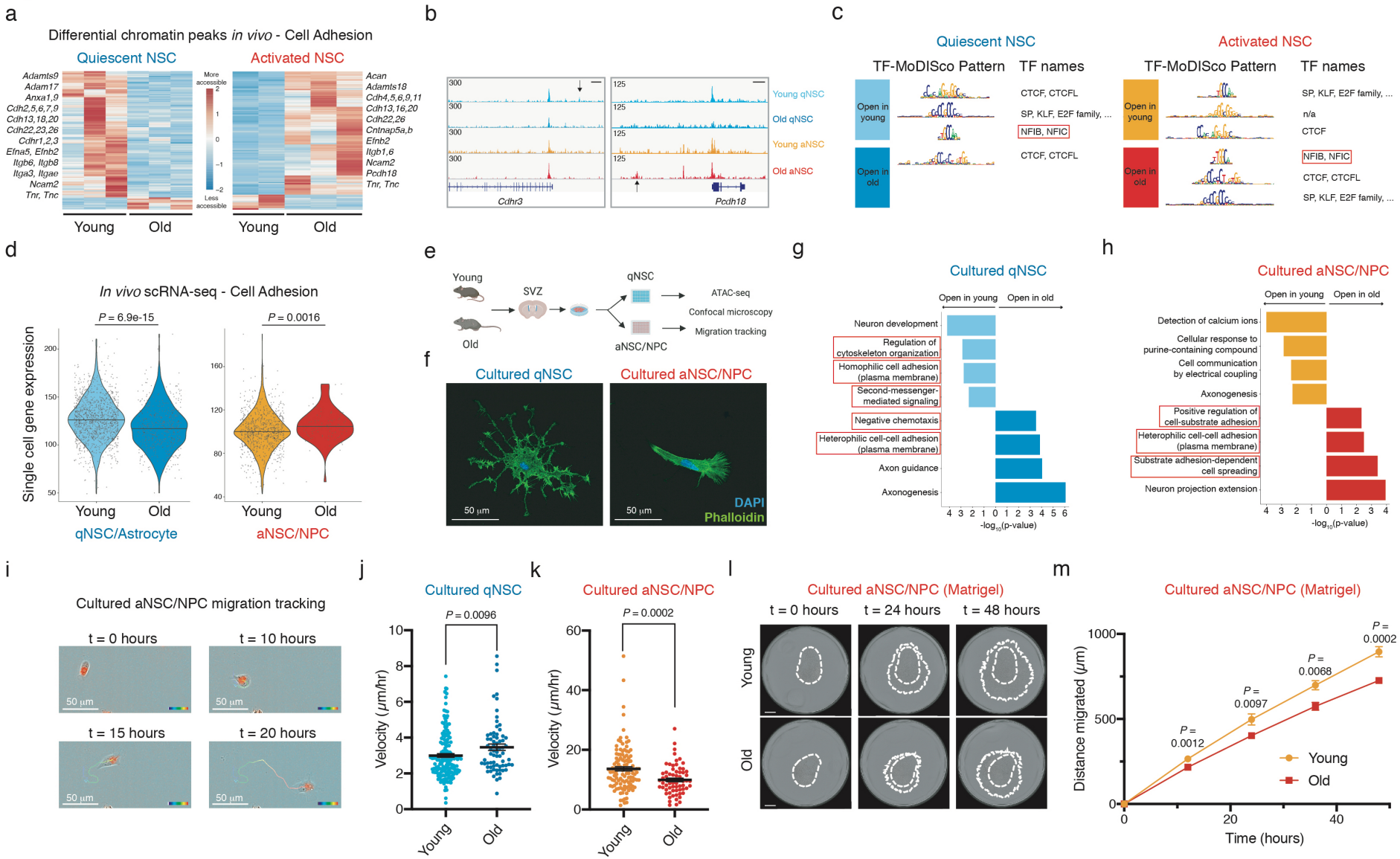

Figure 2: The opposing chromatin changes in old quiescent and activated NSCs with aging are associated with functional defects in cell adhesion and migration

a) Heatmap showing accessibility levels of differential ATAC-seq peaks associated with the "Cell Adhesion" GO category (GO:0007155) that change with age in qNSCs (left) and aNSCs (right) respectively. Selected gene names with associated differentially accessible peaks are displayed. TMM-normalized read counts (by EdgeR), scaled row-wise.

b) Genome browser (IGV) view of chromatin accessibility signal tracks from representative RPKM-normalized libraries of quiescent and activated NSCs isolated from young and old brains illustrating differential chromatin peaks that change with age in young quiescent NSCs (left) and old activated NSCs (right) respectively. Black arrows represent sites of differentially accessible peaks that change with age in qNSCs (left) and aNSCs (right) respectively. *Cdhr3*, Cadherin Related Family Member 3. *Pcdh18*, Protocadherin 18. Scale bar, 5kb.

c) Enrichment of top-ranked transcription factor motifs by TF-MoDISco within differentially accessible ATAC-seq peaks that change with age in qNSCs (left) and aNSCs (right). Red box indicates motif associated with NFI family.

d) Violin plots of the average distribution of single cell cumulative expression profiles of genes within the "Cell Adhesion" GO category (GO:0007155) for young and old qNSCs/astrocytes (left) and aNSCs/NPCs (right) from scRNA-seq data[25]. Each overlaid dot represents the cumulative expression of cell adhesion genes in a single cell. *P*-values were calculated using a two-tailed Mann-Whitney test.

e) Schematic illustrating the general protocol for experiments involving cultured qNSCs and aNSCs/NPCs. Young (3-5 months) and old (20-24 months) C57BL/6 SVZs were microdissected and tissues were processed to enable NSC culture. Quiescence was induced with growth factors bFGF and BMP4 for 5-10 days, and activation was maintained with bFGF and EGF for 1-2 days prior to downstream experiments (ATAC-seq library generation, confocal microscopy, and live-cell migration tracking).

f) Representative images of immunofluorescence staining of a young (3 months) qNSC (left) and aNSC/NPC (right) cultured on Poly-D-Lysine. Blue, DAPI (nuclei); green, phalloidin (F-actin). Scale bar, 50 μm.

g,h) Selected GO terms for genes associated with differentially accessible ATAC-seq peaks (FDR<0.05) that change with age in cultured qNSCs (g) and aNSCs/NPCs (h) generated by EnrichR and ranked by *P*-value. Red boxes indicate GO terms associated with cell adhesion and cell migration.

i) Representative images of a young (3-4 months) aNSC/NPC in the presence of cell-permeant red fluorescent nucleic acid stain Syto64 taken at t = 0, 10, 15, and 20 hours after sorting onto Poly-D-Lysine. The Incucyte system was used for 20x imaging and migration tracks were determined using Imaris (v9.3.0). Color gradient bar represents the passage of time from 0 (blue) to 20 (red) hours. Scale bar, 50 μm.

j) Migration speed of young (3-4 months) and old (23-24 months) qNSCs on Poly-D-Lysine. Each dot represents the average velocity of a single cell over a 20-hour period (n = 6 young male mice, and n = 4 old male mice) (combined over 2 experiments). Data are mean ± SEM. *P*-values were calculated using a two-tailed Mann-Whitney test.

k) Migration speed of young (3-4 months) and old (21-24 months) aNSCs/NPCs on Poly-D-Lysine. Each dot represents the average velocity of a single cell over a 20-hour period (n = 9 young male mice, and n = 7 old male mice) (combined over 3 experiments). Data are mean ± SEM. P-values were calculated using a two-tailed Mann-Whitney test.

l) Representative images of young (top) and old (bottom) aNSC/NPC invasion through Matrigel taken 0, 24, and 48 hours after seeding aNSCs/NPCs. The dotted white outline represents the outermost extent of invasion and the inner dotted white line represents the initial extent of the cells after seeding (t = 0 hours). Scale bar, 800 μm.

m) Migration distance timecourse of young (3-4 months) and old (21-24 months) aNSC/NPC invasion through Matrigel over 48 hours with 12-hour intervals. (n = 7 young male mice, and n = 10 old male mice) (combined over 2 experiments). For each biological replicate, 1-4 technical replicates were evaluated, and migration distance was averaged at each timepoint. Data are mean ± SEM. P-values were calculated at each timepoint using a two-tailed Mann-Whitney test.

Figure 3

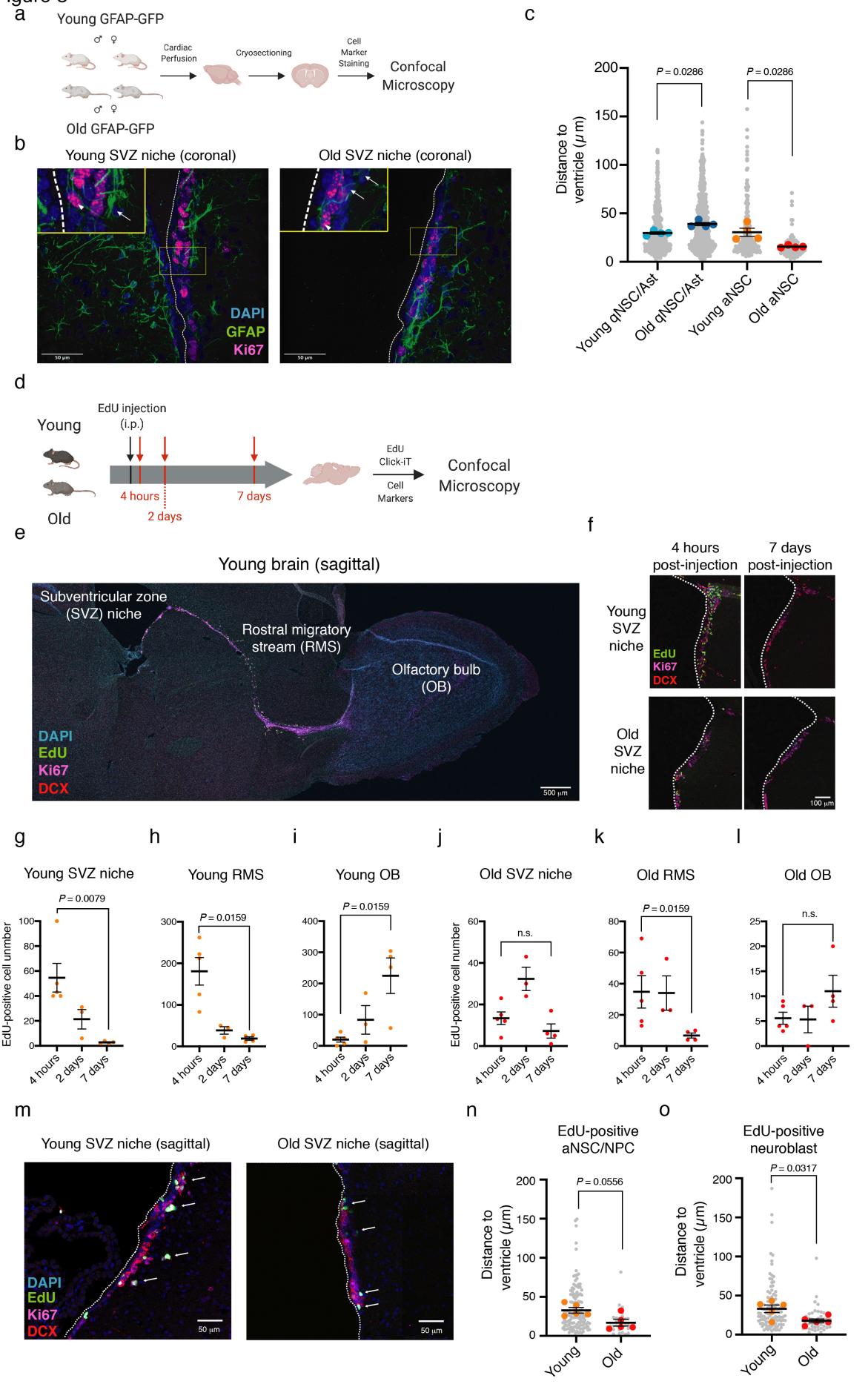

Figure 3: Age-dependent cell adhesion and migration defects of quiescent and activated NSCs and progenitors *in vivo*

a) Design of immunofluorescence experiments for quantifying the localization of qNSCs/astrocytes and aNSCs *in vivo* during aging in coronal brain sections. Young (4 months) and old (18-26 months) mixed-sex GFAP-GFP animals were perfused with 4% PFA, brains were cryosectioned at a thickness of 16 μm and stained for cell markers prior to quantification with confocal microscopy.

b) Representative images of immunofluorescence staining of coronal SVZ sections from young (4 months) (left) and old (18-26 months) (right) GFAP-GFP brains. Yellow box denotes inset containing qNSCs/astrocytes (GFAP+/Ki67-) and aNSCs (GFAP+/Ki67+) indicated with white arrows and arrowheads, respectively. The ventricular lining is indicated by a dotted white line. Blue, DAPI (nuclei); green, GFAP (Astrocyte/NSC marker); pink, Ki67 (proliferation marker). Scale bar, 50 μm.

c) NSC distance to the ventricle was calculated for qNSCs/astrocytes (GFAP+/Ki67-) and aNSCs (GFAP+/Ki67+) in coronal sections of young (4 months) and old (18-26 months) SVZs. Each gray dot represents the distance of a single cell from the ventricular lining and each colored dot represents the mean distance from the ventricle per animal (n = 4 mixed-sex young mice, and n = 4 mixed-sex old mice) (combined over 4 paired young/old experiments). Data are mean ± SEM. Ast, astrocytes. *P*-values were calculated using a two-tailed Mann-Whitney test comparing sample means between conditions.

d) Design of immunofluorescence experiments to assess EdU-labelled NSC migration out of the SVZ *in vivo*. Young (2-3 months) and old (21 months) C57/BL6 male animals were

intraperitoneally injected with EdU, and then sacrificed and perfused with 4% PFA after a time interval of 4 hours, 2 days, or 7 days. Perfused brains were sagittally cryosectioned at a thickness of 16 μm and stained for EdU and cell markers prior to quantification with confocal microscopy. EdU, 5-Ethynyl-2'-deoxyuridine. I.p., intraperitoneal.

e) Representative immunofluorescence staining of sagittal sections encompassing the subventricular zone (SVZ) niche, rostral migratory stream (RMS), and olfactory bulb (OB) of a young (2-3 months) male C57BL/6 mouse 4hrs after intraperitoneal EdU injection. Blue, DAPI (nuclei); green, EdU (proliferation marker); pink, Ki67 (aNSC/NPC/neuroblast marker); red, DCX (neuroblast marker). Scale bar, 500 μm.

f) Representative image of immunofluorescence staining in sagittal sections of the SVZ niche from a young (2-3 months) (top) or old (21 months) (bottom) male C57BL/6 mouse 4hrs (left) or 7 days (right) after intraperitoneal EdU injection. The ventricular lining is indicated by a dotted white line. Green, EdU (proliferation marker); pink, Ki67 (aNSC/NPC/neuroblast marker); red, DCX (neuroblast marker). Scale bar, 100 μm.

g,h,i) Quantification of EdU+ cells counted in the SVZ (g), RMS (h), and OB (i) from young (2-3 months) sagittal sections 4 hours, 2 days, and 7 days post-injection of EdU. Each colored dot represents the number of EdU+ cells counted in a sagittal section from a single animal (n = 5 young male mice 4 hours post-injection, n = 3 young male mice 2 days post-injection, n = 4 young male mice 7 days post-injection) (combined over 2 experiment). Data are mean ± SEM. P-values were calculated using a two-tailed Mann-Whitney test.

j,k,l) Quantification of EdU+ cells counted in the SVZ (j), RMS (k), and OB (l) from old (21 months) sagittal sections 4 hours, 2 days, and 7 days post-injection of EdU. Each colored dot represents the number of EdU+ cells counted in a sagittal section from a single animal (n = 5

old male mice 4 hours post-injection, *n* = 3 old male mice 2 days post-injection, *n* = 4 old male mice 7 days post-injection) (combined over 2 experiment). Data are mean ± SEM. *P*-values were calculated using a two-tailed Mann-Whitney test.

m) Representative images of immunofluorescence staining of sagittal SVZ sections of young (2-3 months) (left) and old (21 months) (right) male C57BL/6 mice 4hrs after intraperitoneal EdU injection. Blue, DAPI (nuclei); green, EdU (proliferation marker); pink, Ki67 (aNSC/NPC/neuroblast marker); red, DCX (neuroblast marker). Dotted white line indicates ventricle wall and white arrows indicate selected EdU-positive cells. Scale bar, 50 μm.

n) Distance to the ventricle was calculated for EdU+ aNSCs/NPCs (Ki67+/DCX-) in sagittal sections of young (2-3 months) and old (21 months) SVZs 4 hours after EdU injection. Each gray dot represents the distance of a single aNSC/NPC from the ventricle and each colored dot represents the mean aNSC/NPC distance from the ventricle per animal (*n* = 5 young male mice, and *n* = 5 old male mice) (combined over 2 experiments). Data are mean ± SEM. *P*-values were calculated using a two-tailed Mann-Whitney test comparing sample means between conditions.

o) Distance to the ventricle was calculated for EdU+ neuroblasts (DCX+) in sagittal sections of young (2-3 months) and old (21 months) SVZs 4 hours after EdU injection. Each gray dot represents the distance of a single neuroblast from the ventricle and each colored dot represents the mean neuroblast distance from the ventricle per animal (*n* = 5 young male mice, and *n* = 5 old male mice) (combined over 2 experiments). Data are mean ± SEM. *P*-values were calculated using a two-tailed Mann-Whitney test comparing sample means between conditions.

Figure 4

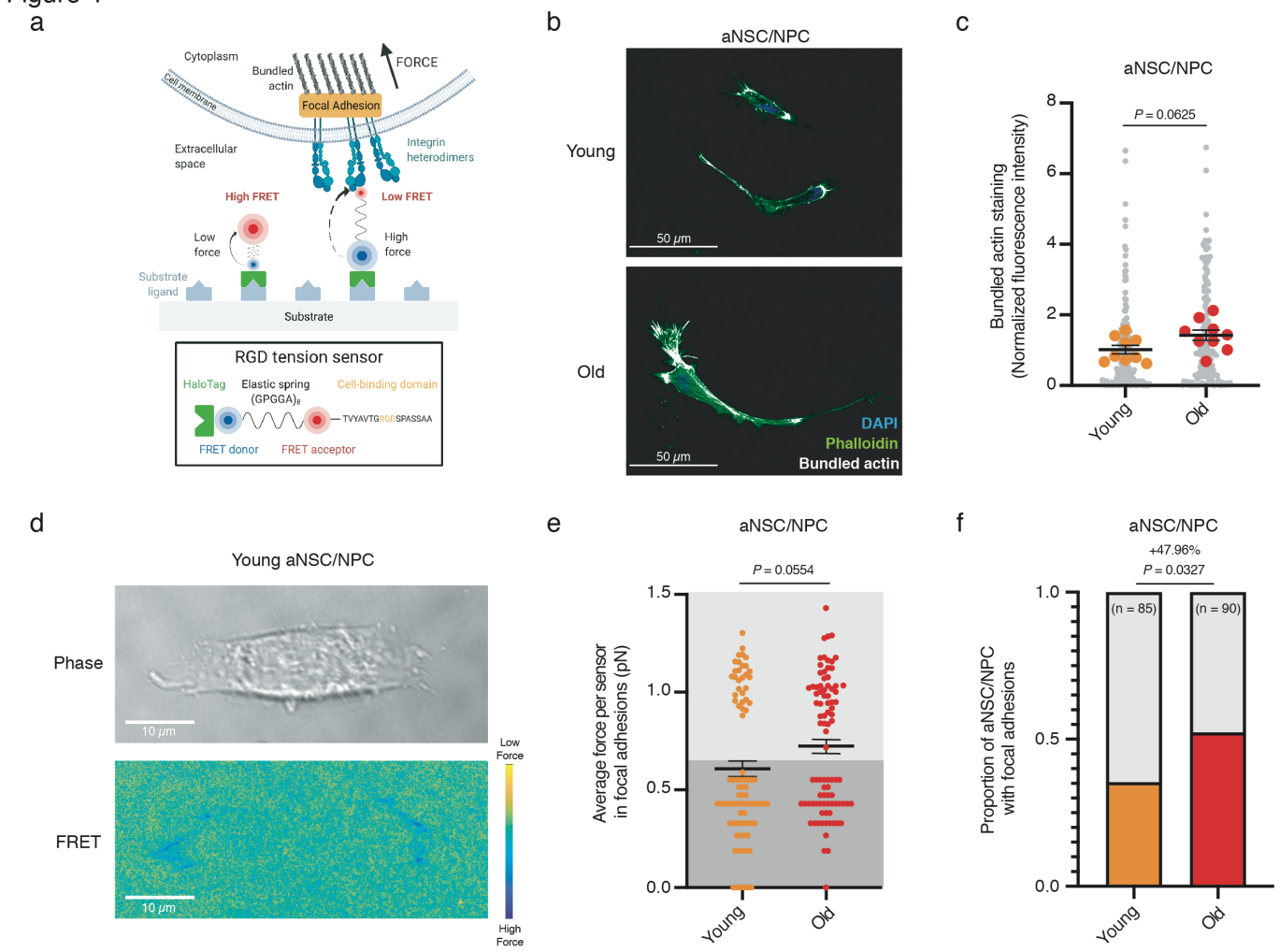

Figure 4: Aging increases the occurrence of force-producing focal adhesions in aNSCs/NPCs

a) Diagram of RGD molecular tension sensor (adapted from previous work[55]). As cells adhere to the tension sensor-coated substrate, integrin heterodimers bind to the RGD cell-binding domain and exert force across a molecular spring, resulting in decreased FRET signal. RGD, peptide containing tripeptide Arg-Gly-Asp motif. FRET, Förster resonance energy transfer.

b) Representative images of immunofluorescence staining of young (3-4 months) (top) and old (21-24 months) (bottom) cultured aNSCs/NPCs on Poly-D-Lysine. Blue, DAPI (nuclei); green, phalloidin (F-actin); white, high-intensity phalloidin mask (bundled actin). Scale bar, 50 μm.

c) Bundled actin fluorescence intensity in young (3-4 months) and old (21-24 months) cultured aNSCs/NPCs, normalized to the mean levels of the young condition. Each gray dot represents bundled actin levels in a single cell and each colored dot represents the average cellular bundled actin level per animal (n = 9 young male mice, and n = 9 old male mice) (combined over 3 experiments). Data are mean ± SEM. P-values were calculated using a two-tailed Mann-Whitney test comparing sample means between conditions.

d) Representative image of a young (3 months) cultured aNSC/NPC seeded on RGD molecular tension sensors taken with phase contrast (top) and FRET donor/acceptor fluorescence wavelengths to generate a high-resolution traction map of FRET efficiency (bottom). The colored bar reflects the FRET efficiency, a measure of adhesion strength, where a low FRET efficiency indicates high force (blue color) and a high FRET efficiency indicates low force (yellow/green color). Scale bar, 10 μm.

e) Average force per sensor (pN) in individual focal adhesions exhibited by young (3 months) and old (21 months) cultured aNSCs/NPCs determined using RGD molecular tension sensors (n = 85 young aNSCs/NPCs, and n = 90 old aNSCs/NPCs) (combined over 2 separate experiments). Shading delineates the bimodal populations of cells with active focal adhesions (light grey, each dot represents the average force sensor reading among focal adhesions for a single cell) or no detected focal adhesion (dark grey, each dot represents the average force sensor reading underneath the cell body). *P*-values were calculated using a two-tailed Mann-Whitney test.

f) Fraction of young (3 months) and old (21 months) cultured aNSCs/NPCs exhibiting focal adhesion patterns as determined from RGD tension sensor experiments (combined over 2 separate experiments). *P*-values were calculated using a combined Fisher's exact test.

Figure 5

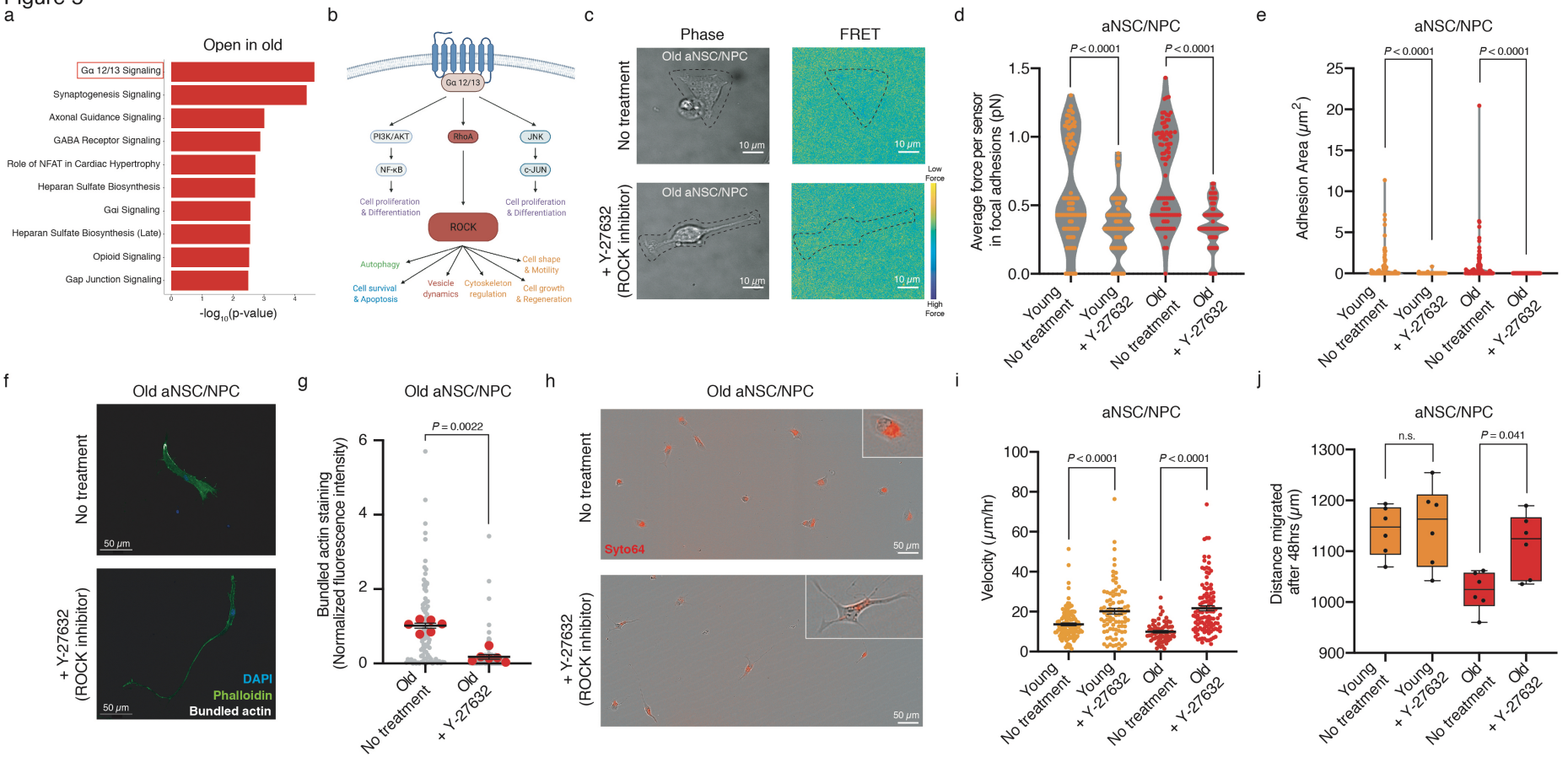

Figure 5: Inhibition of ROCK boosts migration speed and eliminates focal adhesions in aNSCs/NPCs from aged brains

a) Top 10 canonical pathways enriched for genes associated with differentially accessible peaks that open with age in freshly isolated aNSCs (FDR<0.05) generated by Ingenuity Pathway Analysis (IPA) and ranked by *P*-value. ATAC-seq peaks were annotated with their nearest gene using ChIPSeeker (v1.18.0) and *P*-values were calculated using Fisher's Exact Test by IPA.

b) Diagram of the Gα 12/13 signaling pathway with selected targets including ROCK and downstream biological processes regulated by ROCK (adapted from the IPA canonical pathway diagram "Gα 12/13 Signaling" and previous work[86]). RhoA, Ras homolog family member A. ROCK, Rho-associated coiled-coiled kinase. PI3K, phosphoinositide 3-kinase. AKT, AKT serine/threonine kinase 1. NF-κB, Nuclear factor-kappa B. JNK, c-Jun N-terminal kinase.

c) Representative images of old (21 months) cultured aNSCs/NPCs treated with H_2O vehicle (top) or with 10 μM Y-27632 (bottom) seeded on RGD molecular tension sensors taken with phase contrast (left) and FRET donor/acceptor fluorescence wavelengths to generate a high-resolution traction map of FRET efficiency (right). A low FRET efficiency indicates high force (blue color) and a high FRET efficiency indicates low force (yellow/green color). Black dotted lines around the adhered cell bodies were generated using phase contrast images and overlaid onto FRET images. Scale bar, 10 μm.

d) Truncated violin plot of average force per sensor (pN) in individual focal adhesions exhibited by young (3 months) and old (21 months) cultured aNSCs/NPCs treated with H_2O vehicle or

with 10 μM Y-27632 determined using RGD molecular tension sensors (*n* = 85 young aNSCs/NPCs, *n* = 54 young aNSCs/NPCs + 10 μM Y-27632, *n* = 90 old aNSCs/NPCs, and *n* = 74 old aNSCs/NPCs +10 μM Y-27632) (combined over 2 separate experiments). For cells exhibiting focal adhesion patterns, each dot represents the average force sensor reading among focal adhesions for a single cell. For cells without any focal adhesions, each dot represents the average force sensor reading underneath the cell body. *P*-values were calculated using a two-tailed Mann-Whitney test.

e) Truncated violin plot of adhesion area under focal adhesions of young (3 months) and old (21 months) aNSCs/NPCs treated with H_2O vehicle or with 10 μM Y-27632 determined using RGD molecular tension sensors (*n* = 85 young aNSCs/NPCs, *n* = 54 young aNSCs/NPCs + 10 μM Y-27632, *n* = 90 old aNSCs/NPCs, and *n* = 74 old aNSCs/NPCs +10 μM Y-27632) (combined over 2 separate experiments). Each dot represents the adhesion area of force-producing focal adhesions for a single cell. *P*-values were calculated using a two-tailed Mann-Whitney test.

f) Representative images of immunofluorescence staining of an old (21-23 months old) aNSC/NPC treated with H_2O vehicle (top) or with 10 μM Y-27632 (bottom) cultured on Poly-D-Lysine. Blue, DAPI (nuclei); green, phalloidin (F-actin); white, high-intensity phalloidin mask (bundled actin). Scale bar, 50 μm.

g) Fluorescence intensity of bundled actin in old (21-23 months) aNSCs/NPCs treated with H_2O vehicle or with 10 μM Y-27632 cultured on Poly-D-Lysine, normalized to the mean levels of the untreated condition. Each gray dot represents bundled actin levels in a single cell and each colored dot represents the average cellular bundled actin level per animal (*n* = 6 old cultures for both untreated and treated conditions) (combined over 2 experiments). Data are

mean ± SEM. *P*-values were calculated using a two-tailed Mann-Whitney test comparing sample means between conditions.

h) Representative images of old (21-24 months) cultured aNSCs/NPCs 12 hours after sorting onto Poly-D-Lysine-coated migration plates treated with H_2O vehicle (top) or 10μM Y-27632 (bottom). Images were taken with the Incucyte S3 system with phase contrast and RFP imaging overlaid. Live cells were stained with Syto64, a cell-permeant red fluorescent nucleic acid stain, for migration tracking. Outlined inset (top-right) displays a representative magnified cell. Scale bar, 50 μm.

i) Migration speed of young (3-4 months) and old (21-24 months) aNSCs/NPCs cultured on Poly-D-Lysine treated with H_2O vehicle or with 10 μM Y-27632. Each dot represents the average velocity of a single cell over a 20-hour period ($n = 9$ young control cultures, $n = 9$ young treatment cultures, $n = 7$ old control cultures, $n = 9$ old treated cultures) (combined over 3 experiments). Data are mean ± SEM. *P*-values were calculated using a two-tailed Mann-Whitney test.

j) Distance migrated through Matrigel after 48 hours by young (3-4 months) and old (21-23 months) cultured aNSCs/NPCs treated with H_2O vehicle or with 10 μM Y-27632. Each dot represents the distance migrated by a single biological replicate after 48 hours ($n = 6$ young cultures for treated and untreated conditions, $n = 6$ old cultures for treated and untreated conditions) (combined over two experiments). For each biological replicate, 1-4 technical replicates were evaluated, and migration distance was averaged. *P*-values were calculated using a two-tailed Mann-Whitney test.